9-18-2017

Molecular Structure and Confining Environment of Sn Sites in Single-Site Chabazite Zeolites

James W. Harris
Purdue University, harris21@purdue.edu

Wei-Chih Liao

John R. Di Iorio
Purdue University

Alisa M. Henry
Purdue University

Ta-Chung Ong

See next page for additional authors

Molecular Structure and Confining Environment of Sn Sites in Single-Site Chabazite Zeolites

James W. Harris,[1,‡] Wei-Chih Liao,[2,‡] John R. Di Iorio,[1] Alisa M. Henry,[1] Ta-Chung Ong,[2,†] Aleix Comas-Vives,[2] Christophe Copéret,[2,*] Rajamani Gounder[1,*]

[1]*Charles D. Davidson School of Chemical Engineering, Purdue University, 480 Stadium Mall Drive, West Lafayette, IN 47907, USA*

[2]*Department of Chemistry and Applied Biosciences, ETH-Zürich, Vladimir-Prelog-Weg 1-5, 8093 Zürich, Switzerland*

ABSTRACT: Chabazite (**CHA**) molecular sieves, which are industrial catalysts for the selective reduction of nitrogen oxides and the conversion of methanol into olefins, are also ideal materials in catalysis research because their crystalline frameworks contain one unique tetrahedral-site. The presence of a single lattice site allows for more accurate descriptions of experimental data using theoretical models, and consequently for more precise structure-function relationships of active sites incorporated into framework positions. A direct hydrothermal synthesis route to prepare pure-silica chabazite molecular sieves substituted with framework Sn atoms (Sn-**CHA**) is developed, which is required to predominantly incorporate Sn within the crystalline lattice. Quantitative titration with Lewis bases (NH_3, CD_3CN, pyridine) demonstrates that framework Sn atoms behave as Lewis acid sites, which catalyze intermolecular propionaldehyde reduction and ethanol oxidation, as well as glucose-fructose isomerization. Aqueous-phase glucose isomerization turnover rates on Sn-**CHA** are four orders-of-magnitude lower than on Sn-Beta zeolites, but similar to those on amorphous Sn-silicates. Further analysis of Sn-**CHA** by dynamic nuclear polarization enhanced solid-state nuclear magnetic resonance (DNP NMR) spectroscopy enables measurement of ^{119}Sn NMR chemical shift anisotropy (CSA) of Sn sites. Comparison of experimentally determined CSA parameters to those computed on cluster models using density functional theory supports the presence of closed sites (Sn-(OSi≡)$_4$) and defect sites ((HO)-Sn-(OSi≡)$_3$) adjacent to a framework Si vacancy), which respectively become hydrated hydrolyzed-open sites and defect sites when Sn-CHA is exposed to ambient conditions or aqueous solution. Kinetic and spectroscopic data show that large substrates (e.g., glucose) are converted only on Sn sites located within disordered mesoporous voids of Sn-**CHA**, which are selectively detected and quantified in IR and ^{15}N and ^{119}Sn DNP NMR spectra using pyridine titrants. This integrated experimental and theoretical approach allows precise description of the primary coordination and secondary confining environments of Sn active sites isolated in crystalline silica frameworks, and clearly establishes the role of confinement within microporous voids for aqueous-phase glucose isomerization catalysis.

1. Introduction

Single-site heterogeneous catalysts contain active sites that behave uniformly as a result of site isolation and well-defined structures. Their catalytic behavior depends on their local coordination, defined by the bonding of sites to the support and to ancillary ligands,[1-5] which provides a primary environment that influences the electronic properties of the active sites.[1,2,6-8] Their catalytic behavior also depends on their secondary environments, which can result from organic ligands,[1,2,6-8] or from confinement of sites within an inorganic cavity that provides enthalpic and entropic stabilization of bound reactive intermediates through van der Waals and electrostatic interactions.[9-12] As a result, accurate descriptions of catalytic active sites require precise definitions of both the local structure and the secondary environments of the binding sites, in turn, requiring spectroscopic and kinetic probes sensitive to both environments.

Zeolites belong to one of the most widely used and studied classes of heterogeneous catalysts[13,14] for which primary and secondary environments influence catalytic reactivity. The substitution of some silicon atoms in the crystalline zeolite lattice with heteroatoms provides a route to prepare single-site catalysts that contain isolated metal atoms with well-defined local structures and confining environments. Among siliceous frameworks containing tetravalent heteroatoms (M^{4+} = Sn, Ti, Zr, Hf), Sn-Beta zeolites have received considerable attention because of their ability to catalyze a broad range of reactions including the Baeyer-Villiger oxidation of ketones,[15] the intermolecular Meerwein-Ponndorf-Verley oxidation of alcohols and Oppenauer reduction of aldehydes (MPVO),[16] and the related intramolecular MPVO cycle of glucose-fructose isomerization.[17] Different four-coordinate Sn local structures have been proposed, including "closed" sites with four framework bonds [Sn-(OSi≡)$_4$] and "open" sites with three framework bonds and an OH ligand [(HO)-Sn-(OSi≡)$_3$], which exist as either "hydrolyzed-open" (adjacent ≡Si-OH) or "defect" sites (adjacent to a framework Si vacancy) (Scheme 1). Closed and open Sn sites have been identified using IR and ^{119}Sn solid-state NMR spectroscopy together with density functional theory (DFT) calculations,[18,19] and their detailed local structures in Sn-Beta zeolites have been refined by the combined use of dynamic nuclear polarization enhanced solid-state NMR (DNP NMR) and DFT calculations.[20] DNP is used to significantly enhance the NMR sensitivity utilizing microwave-promoted polarization transfer from unpaired electrons to nuclei, typically protons,[21-23] whose hyperpolarization can be transferred to the targeted heteroatoms (e.g., ^{119}Sn)[20,24-26] through cross-polarization (CP). DNP enables acquiring ^{119}Sn chemical shift anisotropy (CSA) parameters at natural abundance, which can be compared to values calculated from DFT to discriminate local Sn structure and location.[27] In the case of Sn-Beta zeo-

lites, however, precise structural assignments are complicated by the presence of different metal-framework coordination modes, multiple tetrahedral-site (T-site) locations[27,28] and crystal polymorphs,[29] and the inhomogeneous spatial distribution of Sn throughout crystallites.[30]

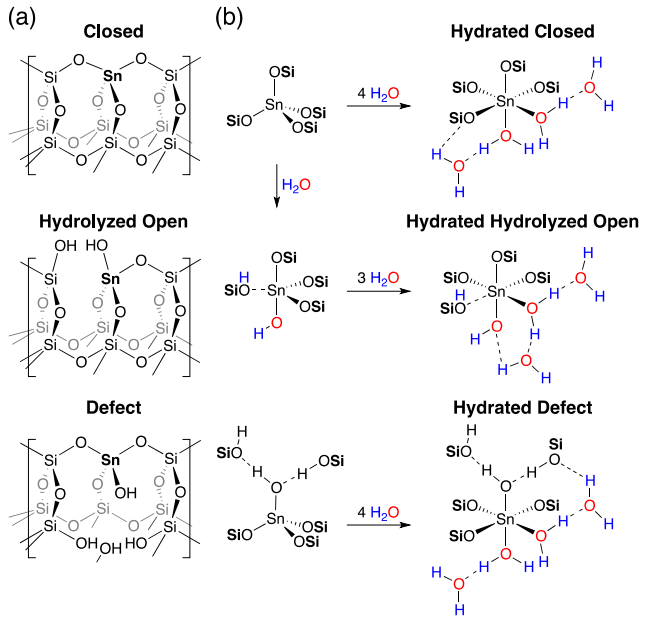

Scheme 1. Depictions of (a) framework Sn structures (closed, hydrolyzed-open, and defect) that may be present in Sn zeolites, and (b) the proposed molecular structures of Sn sites under dehydrated and hydrated conditions.

In contrast to most molecular sieves, chabazite (**CHA**) is a high-symmetry framework containing only one crystallographically unique T-site, which promises to clarify interpretations of experimental characterization data and to provide model structures that can be described more accurately by theory. Periodic DFT studies of metal-substituted zeolites have estimated Ti heteroatom stability in **CHA**,[31] and compared adsorbate (water, ammonia, pyridine) binding energies at various heteroatom sites in **CHA**.[32-35] Such studies have also estimated ammonia binding energies,[36] and developed linear scaling relationships for O- and S-containing compounds,[37] bound at different heteroatoms in **CHA**. Theoretical studies of metal-substituted **CHA** frameworks continue to proliferate, yet experimental progress to prepare and characterize such model catalysts has not been commensurate.

Here, we report the direct hydrothermal synthesis of siliceous **CHA** zeolites containing framework Sn atoms, their catalytic function as solid Lewis acids for substrates of varying size, and the detailed structural characterization of Sn active sites that distinguishes their primary and secondary environments. The single T-site nature of Sn-**CHA** allows more accurate theoretical modeling, and the use of CD_3CN titrants enables quantifying different Lewis acidic Sn structures detected by bulk spectroscopic techniques. We provide evidence that Sn-**CHA** catalyzes the MPVO reaction of propionaldehyde and ethanol, yet is essentially unreactive for glucose isomerization. The combination of DNP NMR with DFT calculations enables identifying different local Sn structures (closed vs. open vs. defect), while the combination of IR and DNP NMR with pyridine titrants (ca. 0.6 nm diameter), which are unable to traverse eight-membered ring **CHA** apertures (ca. 0.4 nm diam.), enables probing different secondary confining environments in **CHA** (microporous vs. mesoporous voids) and establishing a structure-reactivity relationship that highlights the critical role of microporous confining environments around Sn sites for aqueous-phase glucose-fructose isomerization.

2. Experimental and Theoretical Methods

2.1. Catalyst Synthesis

In each of the synthesis procedures reported in this section, reagents were used without further purification.

Sn-**CHA** molecular sieves were synthesized by adapting the procedure reported for the synthesis of Ti-**CHA** by Eilertsen et al.[38] In a typical synthesis, 40 g of ethanol (200 proof, Koptec) were added to a perfluoroalkoxy alkane (PFA, Savillex Corp.) container, followed by addition of 25 g of tetraethylorthosilicate (TEOS, 98 wt%, Sigma Aldrich) and then stirring for 300 s under ambient conditions. Next, a solution containing 0.601 g of $Sn(IV)Cl_4(H_2O)_5$ (98 wt%, Sigma Aldrich) dissolved in 10 g of ethanol was added dropwise to the mixture comprised of TEOS and ethanol, and then stirred for 300 s under ambient conditions. After this period of homogenization, 0.577 g of hydrogen peroxide (H_2O_2, 30 wt%, Alfa Aesar) were added dropwise and the solution was stirred for 900 s under ambient conditions. Next, 42.329 g of an aqueous N,N,N-trimethyl-1-adamantylammonium hydroxide solution (TMAdaOH, 25 wt%, Sachem), the structure directing agent for CHA, were added dropwise to the Sn-containing solution under constant stirring. The solution gelatinized after approximately 15-20 g of TMAdaOH were added, and was hydrated with 49.920 g of deionized water (18.2 MΩ) and manually stirred with a Teflon spatula until a uniform solution was obtained. The remaining TMAdaOH was added dropwise and no further gelatinization occurred. The resulting solution was covered and stirred at ambient temperature for 24 h.

After this period of time, the solution was uncovered and ethanol (61.65 g, including that generated by hydrolysis of TEOS) and excess water (77.78 g) were allowed to evaporate to reach the target weight and desired H_2O/SiO_2 ratio of 3. This resulted in a dry powder that was rehydrated with approximately 80 g of water (18.2 MΩ), stirred for 24 hours to obtain a homogeneous solution, and dehydrated again to reach the desired H_2O/SiO_2 ratio of 3. Attempts to crystallize Sn-**CHA** without this intermediate rehydration step resulted in amorphous products, even after extended periods of time in the synthesis oven (up to 10 days at 423 K). Next, 2.69 g of hydrofluoric acid (HF, 48 wt%, Alfa Aesar) were added dropwise to the synthesis powder and stirred manually with a Teflon spatula for 300 s and residual HF allowed to evaporate for an additional 900 s. ***Caution: when working with hydrofluoric acid use appropriate personal protective equipment, ventilation, and other safety measures.*** The final molar composition of the synthesis powder was 1 SiO_2/ 0.014 SnO_2/ 0.43 TMAdaOH/ 0.38 HF/ 3 H_2O. The powder was transferred to four Teflon-lined stainless steel autoclaves (45 cm^3, Parr Instruments) and heated at 423 K in an isothermal convection oven (Yamato DKN-402C) with rotation (ca. 40 RPM) for 48 hours.

Pure silica chabazite was synthesized following the procedure reported by Díaz-Cabañas et al.[39] In a typical synthesis, 13 g of TEOS were added to a PFA jar containing 25.849 g of an aqueous TMAdaOH solution and stirred under ambient conditions for 300 s. The vessel was left uncovered and ethanol, formed from the hydrolysis of TEOS, and excess water were evaporated to reach a target H_2O/SiO_2 ratio of 3. This resulted

in a dry powder, at which point an additional 10 g of water were added to ensure complete hydrolysis of TEOS and to allow additional time for residual ethanol to completely evaporate. This rehydration procedure was performed twice. Once the synthesis solution had reached the desired H_2O/SiO_2 ratio of 3, 1.28 g of HF (48 wt%, Sigma Aldrich) were added dropwise to the synthesis and homogenized for 300 s using a Teflon spatula. Upon addition of HF to the powdered synthesis mixture, the powder immediately became a thick paste that liquefied slightly under stirring. The solution was left uncovered under ambient conditions for 900 s to allow for any residual HF to evaporate before transferring the solution to two Teflon-lined stainless steel autoclaves (45 cm^3, Parr Instruments) and heating in a forced convection oven at 423 K under rotation (ca. 40 RPM) for 48 h.

Sn-Beta was prepared in fluoride media by modification of a previously reported method[40] using Si-Beta zeolites as seed material. Sn-Beta zeolites were synthesized using the same procedure as Si-Beta, except that dropwise addition of a solution of 0.30 g of tin (IV) chloride pentahydrate ($SnCl_4$-$5H_2O$, Sigma-Aldrich, 98 wt%) in 1.95 g of deionized water was performed prior to evaporation of ethanol and water, such that the synthesis gel had a molar SiO_2/SnO_2 ratio of 130. After the HF addition step and addition of the Sn-Beta synthesis gel to the Teflon liner, 1.73 g of water and 0.254 g of as-made Si-Beta seeds (ca. 4.2 wt% of total SiO_2) were added directly to the liner and the mixture was stirred manually using a Teflon spatula prior to heating in an isothermal oven held at 413 K for 21 days under rotation at 60 RPM.

The solids obtained from all zeolite syntheses were removed from their Teflon liners, washed thoroughly with water and acetone (Sigma Aldrich, >99.5 wt%, 5 washes each, ca. 25 cm^3 (g zeolite)$^{-1}$ each wash)), isolated by centrifugation, and dried at 373 K for 16 h. The dry zeolite powders were then treated in dry air (Ultra Zero Grade, Indiana Oxygen, 1.67 cm^3 s^{-1} (g zeolite)$^{-1}$) to 853 K (0.0167 K s^{-1}) and held for 10 h in a muffle furnace (Nabertherm LE 6/11 equipped with a P300 controller).

Amorphous Sn-xerogel was synthesized using the procedure reported by van Grieken et al.[41] 5.74 g of a 0.1 M HCl solution (Macron, 37%) were added to a mixture of 52.0 g of TEOS and 67.6 g of deionized water and stirred for 2 h at ambient temperature. Then, 0.77 g of $SnCl_4$-$5H_2O$ were added and the mixture stirred for 1 h. Next, a 1 M NH_4OH solution prepared from concentrated NH_4OH (Sigma Aldrich, 28%-30 wt% NH_3 basis) was added dropwise until the gel point was reached (ca.12 cm^3). The resulting clear gel was dried for 12 h at 433 K. The dried solids were washed with deionized water (5-10 washes, ca. 60 cm^3 per wash) until a constant pH was reached, dried for 12 h at 433 K, and then treated in air (Ultra Zero Grade, Indiana Oxygen, 1.67 cm^3 s^{-1} (g zeolite)$^{-1}$) to 853 K (0.0167 K s^{-1}) for 10 h in a muffle furnace.

2.2 Zeolite Structural Characterization

The bulk Sn content of each sample in this study was determined using atomic absorption spectroscopy (AAS) performed with a Perkin Elmer AAnalyst 300 Atomic Absorption Spectrometer. A 1000 ppm Sn standard (Alfa Aesar, TraceCERT, +/- 4 ppm) was diluted to create calibration standards, and the instrument was calibrated each day before collecting measurements. Sn absorbance values were measured at 284.0 nm in an acetylene/nitrous oxide flame. Catalyst samples (ca. 0.02 g) were dissolved in 2 g of HF (48 wt%, Alfa Aesar) overnight and then further diluted with 30 g of deionized water, prior to elemental analysis. The Sn weight fractions were used together with the unit cell formula for the Beta framework to estimate the Si/Sn ratio in each sample.

Powder X-ray diffraction (XRD) patterns were collected on a Rigaku Smartlab X-ray diffractometer with an ASC-6 automated sample changer and a Cu Kα x-ray source (1.76 kW). Samples (ca. 0.01 g) were packed within zero background, low dead volume sample holders (Rigaku) and diffraction patterns were measured from 4-40° at a scan rate of 0.0025° s^{-1} with a step size of 0.0052°.

Scanning electron microscopy (SEM) and energy dispersive X-ray spectroscopy (EDS) were performed on a FEI Quanta 3D FEG Dual-beam SEM with an Everhart-Thornlev detector for high vacuum imaging. SEM micrographs were collected in the focused beam operating mode with a voltage of 5 kV and spot size of 3 μm for samples after high temperature oxidative treatment, but without additional preparation (e.g., sputtering with a metal coating to avoid charging of the metal oxide surface). EDS was performed using an Oxford INCA Xstrem-2 silicon drift detector equipped with an Xmax80 window for supplemental elemental analysis. EDS analyses were performed at 20 kV with a 6 μm spot size at a magnification of 3000-6000x.

Ar (87 K) and N_2 (77 K), and H_2O (293 K) adsorption and desorption isotherms were measured using a Micromeritics ASAP2020 Surface Area and Porosity Analyzer. Samples (ca. 0.03 g) were pelleted and sieved to retain 180-250 μm diameter particles prior to analysis. Samples were degassed by heating to 393 K (0.0167 K s^{-1}) under vacuum (<0.005 Torr) for 2 h, then heating to 623 K (0.0167 K s^{-1}) under vacuum for 8 h prior to measurement of adsorption and desorption isotherms. Micropore volumes were determined from a semi-log derivative analysis of Ar and N_2 isotherms ($\partial(V_{ads}/g)/\partial(\log(P/P_0)$ vs. $\log(P/P_0)$) to identify the completion of micropore filling. Reported pore volumes were converted from volumes adsorbed at STP to the number of moles adsorbed and then converted to liquid volumes using the liquid molar densities at their respective adsorption temperatures (Ar: 87 K, 0.0350 mol cm^{-3}, N_2: 77 K, 0.0288 mol cm^{-3}, H_2O: 293 K, 0.0554 mol cm^{-3}). Pore size distributions were determined using non-local density functional theory (NLDFT) treatments or measured Ar adsorption isotherms.

(Scanning) transmission electron microscopy ((S)TEM) measurements were performed on a Talos F200X (FEI; high-brightness gun (XFEG)) at U_{acc} = 200 kV. STEM images (1024 x 1024 pixels) were recorded with a high-angle annular dark field (HAADF) detector. Four silicon drift detectors attached to the Talos F200X microscope allowed recording energy-dispersive X-ray spectroscopic (EDXS) maps with high signal:noise ratio (ca. 10 min measurement times) using the Esprit 1.9 program (Bruker).

2.3. Sn Active Site Characterization

2.3.1. Diffuse reflectance UV-Visible Spectroscopy

Diffuse reflectance UV-Visible (DRUV) spectra were collected on a Varian Cary 5000 UV-VIS-NIR using a Harrick Praying Mantis in-situ diffuse reflectance cell. The following spectra were collected on each sample: (i) after exposure to ambient conditions and held in dry He flow (4.17 cm^3 s^{-1} (g zeolite)$^{-1}$) at ambient temperature ("ambient"); (ii) after subsequent treatment to 523 K (ca. 0.5 K s^{-1}) for 1.8 ks in dry He flow

(4.17 $cm^3\ s^{-1}$ (g zeolite)$^{-1}$) ("dehydrated"); and (iii) after subsequent exposure to a wet He stream (4.17 $cm^3\ s^{-1}$ (g zeolite)$^{-1}$, ca. 3% H_2O, bubbled through a glass saturator containing water at ambient temperature) while cooling to 303 K and holding for 300 s ("rehydrated"). DRUV spectra were collected at a resolution of 10 nm s^{-1}, using poly(tetrafluoroethylene) (PTFE, 1 μm powder, Sigma-Aldrich) as the 100% reflectance standard, and were converted to an absorption spectrum using the Kubelka-Munk (F(R)) function. Tauc plots of $[F(R)h\nu]^2$ vs. hν were used to calculate absorption edge energies (additional details in Section S.6).

2.3.2. Infrared Spectroscopy

IR spectra were collected on a Nicolet 4700 spectrometer equipped with a Hg-Cd-Te (MCT, cooled to 77 K by liquid N_2) detector by averaging 64 scans at 2 cm^{-1} resolution in the 4000 to 400 cm^{-1} range, and were taken relative to an empty cell background reference collected under dynamic vacuum (rotary vane rough pump, Alcatel 2008A, <0.1 Torr) at either 423 K (pyridine) or 303 K (CD_3CN). Self-supporting wafers (0.01-0.03 g cm^{-2}) were sealed within a custom-built quartz IR cell with CaF_2 windows, equipped with resistive heating cartridges (Chromalox) held in a conductive brass block that is encased in an alumina silicate insulating chamber (Purdue Research Machining Services), as described elsewhere.[42] Wafer temperatures were measured within 2 mm of each side of the wafer by K-type thermocouples (Omega). The quartz IR cell was connected to a custom glass vacuum manifold used for sample pretreatment and exposure to controlled amounts of gaseous titrants.

Prior to each IR experiment, sample wafers were treated in flowing dry air (6.66 $cm^3\ s^{-1}$ (g zeolite)$^{-1}$) purified by a purge gas generator (Parker Balston, <1 ppm CO_2, 200 K H_2O dew point) to 823 K (0.083 K s^{-1}) for 1 h, and then held under dynamic vacuum (rotary vane rough pump, Alcatel 2008A, <0.1 Torr) at 823 K for 1 h. Next, the sample wafer was cooled under dynamic vacuum to 303 K for adsorption experiments with CD_3CN, or to 423 K for adsorption experiments with pyridine. Each titrant was purified via freeze-pump-thaw (3 cycles) and introduced to the sample in sequential doses (ca. $2.5*10^{-7}$ mol). Equilibration of the sample with each titrant dose was assumed when the final pressure in the cell remained constant for 180 s. After samples reached equilibrium with a detectable gaseous titrant pressure (0.4-2.0 Torr) dosing was considered complete, and samples were exposed to dynamic vacuum (60 s at 303 K for CD_3CN or 900 s at 423 K for pyridine) to remove gas-phase and weakly-bound species.

IR spectra reported were baseline-corrected and normalized to combination and overtone modes of zeolite Si-O-Si stretches (1750-2100 cm^{-1}). IR peaks for CD_3CN species bound to open (2316 cm^{-1}) and closed (2308 cm^{-1}) Lewis acidic Sn sites,[19] bound to Sn sites in highly-defective oxide surfaces (2287 cm^{-1}), hydrogen-bound to Si-OH sites (2275 cm^{-1}), and physisorbed or gas phase CD_3CN (2265 cm^{-1}) overlapped and required deconvolution into individual components.[40] Similarly, those for pyridine adsorbed at Lewis acidic Sn sites (1450 cm^{-1}) and at SiOH groups (1445 cm^{-1}) required deconvolution prior to quantification. The number of sites titrated by pyridine or CD_3CN on self-supporting sample wafers was estimated from integrated IR peak areas and values using the following equation:

$$\text{Site density } (\mu\text{mol g}^{-1}) = \left(\frac{\text{Integrated Peak Area } (\text{cm}^{-1})}{\text{E } (\text{cm } \mu\text{mol}^{-1})}\right) * \left(\frac{a_{CS}\ (\text{cm}^2)}{\text{m(g)}}\right) \quad (1)$$

where a_{CS} and m are the cross-sectional area and mass of the wafer, respectively.

2.3.3. Ammonia Temperature Programmed Desorption

Ammonia temperature programmed desorption (TPD) was performed using a Micromeritics Autochem II 2920 Chemisorption Analyzer connected to an Agilent 5793N mass selective detector (MSD) to quantify the number of moles of ammonia desorbed from Sn-**CHA**. Sn-**CHA** (ca. 0.03 g, sieved to 180-250 μm) was supported in between two plugs of quartz wool in a quartz U-tube reactor, which was held inside a clamshell furnace. The catalyst was treated in air (25 $cm^3\ s^{-1}$ (g zeolite)$^{-1}$, Indiana Oxygen, Ultra Zero Grade) to 673 K (0.167 K s^{-1}) for 4 h and then cooled to ambient temperature. The sample was then saturated in flowing NH_3 in balance helium (25 $cm^3\ s^{-1}$ (g zeolite)$^{-1}$, 500 ppm gravimetric mixture, Indiana Oxygen) for 12 h, and then weakly bound and physisorbed NH_3 were removed by purging the sample in flowing He (25 $cm^3\ s^{-1}$ (g zeolite)$^{-1}$, Indiana Oxygen, 99.999%) for 8 h at 331 K. After the saturation and purge treatment, which was used previously to quantify the number of Lewis acidic Sn sites in Sn-Beta zeolites,[40] TPD was performed in flowing He (25 $cm^3\ s^{-1}$ (g zeolite)$^{-1}$), with the reactor effluent transported to the MSD via heated lines held at >383 K. After the experiment, a 0.5 cm^3 sample loop was filled with argon (Indiana Oxygen, 99.999%) and injected via flowing He (0.83 $cm^3\ s^{-1}$) to the MSD to quantify the amount of NH_3 desorbed from integrated MSD signals and a calibrated response factor for NH_3 relative to Ar, as reported previously.[43]

2.3.4. DNP NMR Spectroscopy

Hydrated Sn-**CHA** was prepared by high temperature oxidative treatment at 853 K (described in Section 2.1) and exposure of the resulting solids to ambient conditions. Dehydrated Sn-**CHA** was prepared by treatment of the hydrated sample under high vacuum (10^{-4} Torr) to 773 K (0.067 K s^{-1}) overnight. After dehydration, the sample was transferred into an argon-filled glovebox, where all DNP sample preparations were performed. Dehydrated Sn-**CHA** was treated with ^{15}N pyridine by adding 50 μL of ^{15}N-labeled pyridine (99% isotopic enrichment, Cortecnet Inc.) into a suspension of dehydrated Sn-CHA (0.10 g) in anhydrous pentane (ca. 1 cm^3). The mixture was stirred at ambient temperature for 600 s, removed from the argon-filled glovebox under inert conditions, and then exposed to high vacuum (10^{-4} Torr) at ambient temperature for 900 s to remove solvent and excess pyridine. The ^{15}N-labeled pyridine-treated Sn-**CHA** sample was then reintroduced into an argon-filled glovebox, where subsequent DNP sample preparation was conducted. All DNP samples were prepared by impregnating the solids with a 16 mM TEKPol[44] solution in 1,1,2,2-tetrachloroethane (TCE).[45] Each impregnated solid was then packed in its own 3.2 mm sapphire rotor. A Teflon spacer was added within each rotor to contain the impregnated solid, and the rotors were then closed with zirconia drive caps.

The DNP NMR measurements were performed either using a Bruker 400 MHz (9.4 T) or a Bruker 600 MHz (14.1 T) DNP spectrometer coupled with corresponding gyrotron microwaves emitting at 263 and 395 GHz located at CRMN Lyon and ETH Zürich, respectively. All experiments were per-

formed using 3.2 mm HXY or HX low temperature magic-angle spinning (LTMAS) probes operating at 100 K. Cross-polarization (CP) MAS experiments with ^{1}H ramped spin-lock pulse were used to transfer the DNP hyperpolarization from ^{1}H to heteronuclei (^{15}N, ^{29}Si, and ^{119}Sn). The spin-lock pulses were optimized matching the Hartmann-Hahn condition under MAS with minor adjustment to maximize the CP efficiency experimentally. The ^{1}H 90° excitation and decoupling pulses were optimized and set to 100 kHz. DNP polarization build-up time constant (T_{DNP}) was measured using saturation-recovery experiments with microwaves on, and the recycle delays of all measurements were set to 1.3*T_{DNP}. For variant DNP build-up time experiments, the recycle delay were chosen as 1, 1.3*T_{DNP}, 10, and, 20 seconds. 2D CP magic-angle turning (MAT) spectra were acquired with the 5-π pulse sequence of Grant and co-workers.[46] Extractions of NMR spectra at the corresponding isotropic chemical shift in the isotropic dimensions were fit using the solid lineshape analysis (SOLA) feature in Bruker's Topspin program in order to determine CSA parameters.

2.4. Density Functional Theory Calculations

The structures of the Sn-**CHA** cluster and their corresponding hydrated and pyridine-coordinated structures were fully optimized with B3LYP[47-50] including D3 empirical dispersion corrections and Becke-Johnson damping[51-52] using the Gaussian 09 code.[53] Solvent (water) effects were included for the hydrated systems optimizing by means of the Polarizable Continuum Model (PCM) method.[54-56] A combination of different basis sets was used to obtain the ground-state geometries and energies. Sn was described by the LanL2DZ effective core pseudopotential (ECP)[57-59] augmented with a *d* polarization function; the O and N atoms directly bonded to Sn were described by a 6-31+G(d) basis set, while Si, C, H, and the remaining O atoms were described by the 6-31G(d,p) basis set. In the optimization, only Si and O atoms forming part of the rings containing the Sn atom were allowed to relax.

Calculations of the NMR parameters[60-61] were carried out at the B3LYP-D3 level as implemented in the ADF code (2012).[62] The all-electron TZP basis set[63] was used for all atoms in the NMR parameter calculations. Relativistic effects and spin−orbit couplings were taken into account through the ZORA method[64-65] for the calculations of the isotropic chemical shift (δ_{iso}) and the principal components (δ_{11}, δ_{22}, and δ_{33}) of all considered species. For the calculations of δ_{iso}, the chemical shieldings of $Sn(CH_3)_4$ and CH_3NO_3 were used as references for ^{119}Sn and ^{15}N, respectively. This methodology has been previously tested for molecular and surface Sn species and showed excellent agreement with experiments within 10-15 ppm for ^{119}Sn NMR.[66]

2.5. Kinetic Studies of MPVO Reactions with Sn-**CHA**

2.5.1 Intramolecular MPVO with glucose

Intramolecular MPVO reactions were performed in batch reactors using 1% (w/w) D-glucose (Sigma Aldrich, ≥99.5%) solutions prepared in deionized water (18.2 MΩ) with the pH controlled to 2 with hydrochloric acid (Macron, 37% (w/w)) to suppress background reactions. Catalysts (Sn-**CHA** and Sn-xerogel: ca. 0.1 g; Sn-Beta: 0.01 g, diluted 1:9 in Si-**CHA**-F) were added to glass reactors (10 cm^3, VWR) and sealed with crimp-tops (PTFE/silicone septum, Agilent) before heating to 398 K atop a digital stirred hotplate (IKA RCT basic). Reactant solutions (ca. 2 cm^3) were pre-heated separately (600 s) and then injected to the capped, preheated reactors, and stirred at 750 rpm under autogenous pressure for either 600 s (Sn-Beta) or 6 h (Sn-**CHA**, Sn-xerogel) prior to quenching in an ice bath. The obtained solutions were filtered with 0.2 µm PTFE filters and mixed with a 1% (w/w) aqueous D-mannitol solution (Sigma-Aldrich ≥98%) used as an internal standard. Product analysis was performed using an Agilent 1260 high performance liquid chromatograph (HPLC) with a Hi-Plex Ca column (7.7 x 300 mm, 8 µm particle size, Agilent) an aqueous mobile phase (0.01 cm^3 s^{-1}, 353 K), and an evaporative light scattering detector (Agilent 1260 Infinity ELSD).

2.5.2 Intermolecular MPVO with Ethanol and Acetone

Intermolecular MPVO reactions were performed in batch reactors using solutions of 0.05-0.2 M acetone (Sigma-Aldrich, ≥99.9%) and propionaldehyde (Alfa Aesar, 97%) in ethanol (Sigma-Aldrich, ≥99.5%) as the solvent. Control experiments were performed using solutions of acetaldehyde (Sigma-Aldrich, ≥99.5%), isopropanol (Sigma-Aldrich, ≥99.5%), acetone, propionaldehyde, and ethanol. All chemicals were used as received without further purification. Catalysts (ca. 0.02 g) were added to thick-walled glass reactors followed by addition of reactant solutions (2-5 cm^3). Crimp-top sealed reactors were heated at 333 K atop a digital stirred hotplate while stirring at 750 RPM under autogenous pressure for various time intervals (0.25 – 6 h) prior to quenching in an ice bath. Resulting product solutions were filtered through 0.2 µm PTFE filters, and mixed with ca. 30 µL of a 5% (w/w) solution of either 2-butanol (Sigma-Aldrich, ≥99.5%, acetone-ethanol reactions) or n-pentanol (Sigma-Aldrich, >99%, propionaldehyde-ethanol reactions) diluted in ethanol as internal standards. Product analysis was performed using an Agilent 7890 gas chromatograph (GC) equipped with a DB-Wax column (J&W Scientific, 60 m x 530 µm x 1.00 µm) and an Agilent 7693 autosampler. Isotopic labeling studies were performed using propionaldehyde and d_5-ethanol (C_2D_5OH, Cambridge Isotopes, 98%). Product analysis was performed using an Agilent 7890A GC equipped with a DB-Wax column (J&W Scientific, 60 m x 530 µm x 1.00 µm), an Agilent 7693 autosampler, and an Agilent 5975C mass spectrometer. Calibration curves for ethanol, acetone, isopropanol, propionaldehyde, n-propanol, and acetaldehyde were created using standards of known concentration relative to known concentrations of 2-butanol or n-pentanol. Initial rates of product formation were determined by extrapolating to zero time using batch reactions under differential acetone or propionaldehyde conversion (<5%, ca. 900 s).

3. Results and Discussion

3.1. Synthesis of Sn-**CHA** and Bulk Structural Characterization of Stannosilicates

Hydrothermal synthesis routes to prepare pure-silica **CHA** molecular sieves containing framework Sn heteroatoms ([Si,Sn]-**CHA**, or "Sn-CHA") have not been reported previously to our knowledge (although a mixed heteroatom [Si,Sn,Al]-**CHA** has been reported[67]); therefore, syntheses were performed by adapting reported procedures for the fluoride-assisted hydrothermal synthesis of Ti-**CHA**[38] (details in Section 2.1). Generally, synthetic routes for Sn-**CHA** involved first homogenizing the silicon precursor (tetraethylorthosilicate) and the tin precursor (an ethanolic solution of stannic chloride pentahydrate) in an aqueous hydrogen peroxide solution, and then adding the organic structure-directing agent (N,N,N-trimethyl-1-adamantylammonium hydroxide). After a

reaction and homogenization period (24 h), ethanol and excess water were evaporated from this solution to obtain the low water contents typical of fluoride-assisted zeolite crystallization (H_2O/SiO_2 = 3), which required performing one intermediate rehydration (H_2O/SiO_2 = 40) and dehydration cycle; attempts to crystallize Sn-**CHA** without this rehydration cycle were unsuccessful (10 days, 423 K). Finally, aqueous hydrofluoric acid was added as the mineralizing agent to form a powder, which crystallized Sn-**CHA** (2 days, 423 K).

Structural characterization data are listed in Table 1 for all samples in this study. Stannosilicate molecular sieves are labeled Sn-X-Y-Z, where X is the framework type (**CHA** or Beta), Y is the mineralizing agent used (-F: fluoride, -OH: hydroxide), and Z is the silicon-to-tin molar ratio determined from atomic absorption spectroscopy. Powder XRD patterns were used to confirm the intended crystal topologies (Section S.2, Fig. S.1) and that samples did not contain extracrystalline SnO_2 domains larger than 3 nm in diameter.[68] SEM images (Section S.3, Fig. S.2) of Sn-**CHA**-F samples show amalgams of small crystallites with a broad size distribution (0.5-3 μm) and the presence of some amorphous debris located at the external surfaces of crystal domains, while those for Si-**CHA**-F show larger crystals (5-20 μm). Argon (**CHA**) and nitrogen (Beta, xerogel) adsorption isotherms (Section S.4, Fig. S.3 and S.4) were used to determine the micropore volumes reported in Table 1, which were consistent with previous reports for each topology,[69-71] except those measured for Sn-**CHA**-F-60 and Sn-**CHA**-F-70, which were lower (0.15-0.16 $cm^3\ g^{-1}$) than those measured for Si-**CHA**-F and Al-**CHA** (0.20-0.23 $cm^3\ g^{-1}$).[69,70] Ar desorption branches on Sn-**CHA**-F-60 and Sn-**CHA**-F-70, but not on Si-**CHA**, showed Type-H4 hysteresis loops with a characteristic step-down at a relative pressure of ca. 0.4, indicating the presence of disordered mesoporous voids.[72] Non-local density functional theory (NLDFT) treatments of Ar adsorption isotherms used to determine pore size distributions (Section S.4, Figs. S.5-S.6) provide further evidence for mesoporous voids (5-10 nm diam.) in Sn-**CHA**-F samples, but not Si-**CHA**-F. TEM images (Section S.5, Figure S.7) show further evidence for crystalline domains and some disordered mesoporous and amorphous regions in Sn-CHA-F. Replicate synthesis of Sn-**CHA** resulted in samples with different Sn content (Si/Sn = 60 and 70) but otherwise indistinguishable bulk structural characteristics, while the Sn-Beta-F-116 sample studied here is representative of a larger suite of Sn-Beta-F samples (>20) we have studied previously.[40,73]

Diffuse-reflectance UV-visible (DRUV) spectra of Sn-**CHA**-F-70, Sn-Beta-F-116, and Sn-xerogel (Section S.6, Figure S.9) were collected after dehydration treatments (523 K), in order to avoid the ambiguity of interpreting overlapping absorption bands (220-250 nm) for hexacoordinate framework Sn centers with coordinated ligands (e.g., water)[74] and for any Sn located within nanometer-sized non-framework SnO_2 domains.[75-78] DRUV spectra showed dominant absorption bands for isolated tetrahedral Sn in Sn-**CHA**-F-70 (ca. 220 nm) and Sn-Beta-F-116 (ca. 210 nm),[17,74] but also showed broad bands (ca. 250 nm) characteristic of hexacoordinate Sn, reflecting either the presence of minority SnO_2 or incomplete dehydration at 623 K (Fig. S.10; TGA analysis in Section S.8). Absorption edge energies (Table 1) extracted from Tauc plots (Fig. S.11) were characteristic of isolated, tetrahedral Sn in zeolitic frameworks (≥4.1 eV)[77,79] for both Sn-**CHA** samples (4.12-4.33 eV) and for Sn-Beta-F-116 (4.23 eV), and higher than for SnO_2 domains (ca. 3 nm) supported on Si-Beta (4.09 eV).[40] Sn K-edge X-ray absorption spectra (XAS) for Sn-**CHA**-F-70, Sn-Beta-F-116, and Sn-xerogel (Fig. S.14, Supporting Information) indicated average Sn coordination numbers of six (5.7-5.8 ± 0.6) under ambient conditions and four (3.8-4.0 ± 0.4) after dehydration, the behavior expected of framework Sn centers (additional details in Section S.8). The average Sn-O bond length in Sn-**CHA**-F-70 derived from EXAFS (1.96 ± 0.02 Å) was longer than expected from density functional theory (DFT) predictions for closed and defect Sn sites (1.88 Å, Section 3.5), perhaps indicating the presence of residual water in Sn-**CHA**-F-70 at 523 K. These bulk characterization techniques indicate that the Sn-**CHA** and Sn-Beta samples studied here contain predominantly Sn atoms isolated within framework positions. We next use site-sensitive characterization techniques that provide increasing resolution into the molecular-level details of local Sn coordination and geometry.

Table 1. Site and structural characterization data for the samples in this study.

Sample	Si/Sn Ratio (AAS)[a]	Si/Sn Ratio (EDS)[b]	$V_{ads,micro}$ ($cm^3\ g^{-1}$)	DRUV Band Center (nm)[e]	DRUV Edge Energy (eV)[e]
Sn-**CHA**-F-60	59	65	0.16[c]	219	4.33
Sn-**CHA**-F-70	70	65	0.15[c]	223	4.12
Sn-Beta-F-116	116	122	0.23[d]	222	4.23
Sn-xerogel	110	130	0.02[d]	245	4.37
Si-**CHA**-F	n. m.*	n. m.*	0.23[c]	n. m.*	n. m.*

[a]Bulk composition determined by atomic absorption spectroscopy (AAS). [b]Composition determined by energy dispersive X-ray spectroscopy (EDS). [c]Micropore volume determined from Ar adsorption isotherms (87 K). [d]Micropore volume determined from N_2 adsorption isotherms (77 K). [e]Diffuse reflectance UV-Vis spectra (band center at maximum F(R) intensity) and Tauc plots for samples after dehydration at 523 K (Section S.6). *n. m., not measured

3.2. Quantifying Lewis acidic Sn sites using d_3-acetonitrile and pyridine titration and IR spectroscopy

Infrared (IR) spectra of Sn-**CHA** samples saturated with CD_3CN are shown in Figure 1, and used to quantify their number of Lewis acidic Sn sites. Sn-Beta zeolites show ν(C≡N) vibrations characteristic of CD_3CN bound to open (2316 cm^{-1}) and closed (2308 cm^{-1}) Sn sites (Section S.9, Fig. S.15),[19] which were quantified using integrated molar extinction coefficients (E; cm μmol^{-1}) measured previously for these sites.[40] On Sn-**CHA** zeolites, ν(C≡N) vibrations for CD_3CN bound to Lewis acidic Sn sites (2310 cm^{-1}), to extracrystalline Sn[80] or to Si-OH groups next to open Sn sites[81] (2287 cm^{-1};

dominant features in an amorphous xerogel[43]), and to silanol groups (2275 cm^{-1}) increased simultaneously with CD_3CN coverage (Fig. 1a).[40] One convoluted peak at 2310 cm^{-1} for CD_3CN bound to open and closed Lewis acidic Sn sites was observed for Sn-**CHA**-F with increasing CD_3CN coverage (Fig. 1a), as also observed on high-defect Sn-Beta zeolites (Sn-Beta-OH).[73] In contrast, low-defect Sn-Beta-F zeolites show two distinct peaks at 2316 cm^{-1} and 2308 cm^{-1} at different CD_3CN coverages (Fig. S.15).[40,73] Lewis acidic Sn sites were quantified (Table 2) after deconvolution of IR spectra at saturation CD_3CN coverages[40,73] to extract contributions from component peaks for open and closed Sn sites and silanol groups (deconvoluted spectra for Sn-**CHA**-F-60 in Fig. 1b). The concentrations of silanol groups on Sn-**CHA**-F-60 and Sn-**CHA**-F-70 were 2-12× higher than on Sn-Beta-F zeolites.[40] These data are consistent with larger H_2O uptakes measured on Sn-**CHA**-F (0.12-0.15 $cm^3\ g^{-1}$ at P/P_0 = 0.2; Fig. S.4b) than on Si-**CHA**-F (by 7×) and on Sn-Beta-F zeolites (by 13×, on average).

The fraction of Lewis acidic Sn sites (per total Sn) titrated by CD_3CN was unity within experimental error (±20%) in Sn-**CHA**-F-60 (1.18) and Sn-**CHA**-F-70 (1.14), consistent with bulk characterization methods reflecting the predominance of framework Sn sites (Section 3.1). This quantification assumed equimolar binding of CD_3CN to each Sn site, consistent with saturation of Lewis acidic Sn sites below monolayer CD_3CN coverages (per total Sn) during sequential dosing experiments on Sn-Beta zeolites.[40] Equimolar CD_3CN binding stoichiometry to each Sn site is also consistent with the absence of hexacoordinate Sn resonances in ^{119}Sn NMR spectra of Sn-Beta saturated with acetonitrile,[82] and with quantitative titration of Lewis acid sites using pyridine, n-propylamine, and ammonia,[40] the adsorption of which leads to pentacoordinate ^{119}Sn resonances in NMR spectra.[18] Equivalent fractions of Lewis acid sites in Sn-**CHA**-F-60 (1.08, Table 2) and Sn-**CHA**-F-70 (1.20, Table 2) were also quantified by ammonia titration and temperature programmed desorption methods developed previously on Sn-Beta zeolites (Section S.10).[40] These titration data indicate that the Sn-**CHA** samples studied here contain predominantly Lewis acidic Sn sites incorporated within framework locations, and that integrated molar extinction coefficients for IR vibrations of CD_3CN bound at Sn sites in Beta zeolites can also be used to quantify Sn sites in **CHA** zeolites.

Framework Sn sites may be confined within either microporous or mesoporous voids, both of which are detected in Ar adsorption isotherms and TEM images, of Sn-**CHA**. The location of Sn within different confining environments was probed using pyridine as a probe molecule (ca. 0.6 nm), which cannot access microporous voids in **CHA** that are limited by eight-membered ring window apertures (ca. 0.4 nm). Any vibrations observed for pyridine bound to Lewis acidic Sn sites thus reflect Sn atoms located at external crystallite surfaces or within mesoporous voids, similar to previous reports for H^+ sites located in partially-mesoporous Al-**CHA** zeolites synthesized in fluoride media.[83] IR spectra measured after pyridine saturation (423 K) of Sn-**CHA**-F (Section S.9, Fig. S.16) showed prominent peaks at 1450 cm^{-1} and 1610 cm^{-1} reflecting deformation modes of pyridine coordinated to Lewis acid sites,[82] and a minor peak for protonated pyridine at 1545 cm^{-1} (20× smaller area than 1450 cm^{-1} peak) as observed previously for post-synthetically prepared Sn-Beta-OH zeolites.[71] The fraction of Sn sites accessible to pyridine was 0.20 (per total Sn) for both Sn-**CHA**-F-60 and Sn-**CHA**-F-70 (Table 2), using values for the integrated molar extinction coefficient for pyridine adsorbed to Lewis acidic Sn sites (E(1450 cm^{-1})) measured previously for pyridine adsorption on Sn-Beta-F zeolites.[40] The accessibility of 20% of the Sn sites in Sn-**CHA** to pyridine would be consistent with a uniform distribution of Sn among microporous and mesoporous voids of the Sn-**CHA** samples studied here, which show lower than expected micropore volumes (by 20-25%) and the presence of mesoporous voids. Indeed, TEM-EDS data of Sn-**CHA**-F-70 (Section S.5, Figure S.8) indicate that Sn is present in a composition (Si/Sn ~60) similar to that measured by SEM-EDS (~65, Table 1) and AAS (~70, Table 1), and that there is no spatial segregation of Sn in Sn-**CHA** particles. We next use active site-sensitive characterization techniques, in the form of catalytic probe reactions, which directly report on the function of framework Sn sites in Sn-**CHA**.

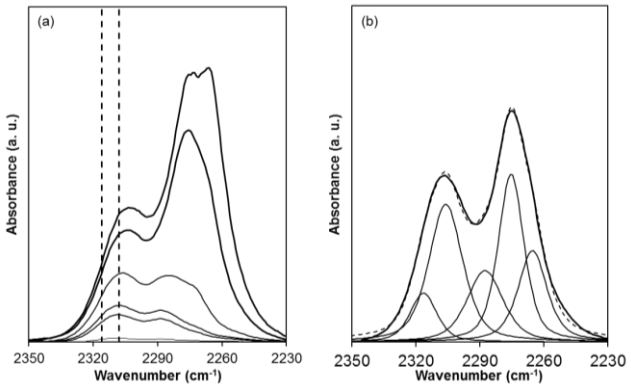

Figure 1. (a) IR difference spectra (relative to zero coverage) of Sn-**CHA**-F-70 upon sequential dosing of CD_3CN to saturation coverages. Vertical dashed lines are shown for open (2316 cm^{-1}) and closed (2308 cm^{-1}) Sn sites. (b) IR spectra of CD_3CN-saturated Sn-**CHA**-F-60, with thin dotted line representing the sum of the component peaks, shown as thin solid lines for CD_3CN bound to open (2316 cm^{-1}) and closed Sn sites (2308 cm^{-1}), Sn sites within high defect surfaces (2287 cm^{-1}), hydrogen bound to SiOH groups (2275 cm^{-1}), and gas phase or physisorbed CD_3CN (2265 cm^{-1}).

3.3. Catalytic interrogation of the confining environment around Sn sites in Sn-**CHA**

3.3.1. Intermolecular propionaldehyde-ethanol MPVO reactions

The Lewis acidic behavior of framework Sn sites of Sn-CHA-F-60 was probed using intermolecular MPVO reactions of ethanol and propionaldehyde, chosen because both molecules (<0.4 nm) can traverse 8-MR **CHA** windows. Intermolecular MPVO reactions proceed via coordination of an alcohol and an aldehyde (or ketone) to a Lewis acid site, subsequent deprotonation of the alcohol, and kinetically-relevant hydride transfer from the alcohol carbon to the carbonyl carbon in a six-membered transition state, as demonstrated experimentally for Lewis acidic Beta zeolites[85] and by theoretical simulations for aluminum alkoxide complexes[86] and Beta zeolites.[87,88] Intermolecular MPVO rate data (333 K) were measured using dilute propionaldehyde solutions in ethanol solvent (0.6 M propionaldehyde), and a representative transient reaction profile is shown in Figure S.18 (Section S.11). 1-Propanol for-

mation rates increased with reaction time and reached 2.75 turnovers (per mol Sn) after 6 h, demonstrating the catalytic nature of Sn sites in Sn-**CHA**-F-60 (Fig. S.18a). 1,1-diethoxy propane, a condensation product of two ethanol molecules and one propionaldehyde molecule, was also detected and is consistent with intermolecular MPVO reactions of ethanol and acetone (discussion in Section S.11) in the presence of solid Lewis acids (e.g., ZrO_2), which catalyze aldol condensation reactions of acetaldehyde products[88-92] with primary alcohols to form acetals.[89] The total formation of 1-propanol and 1,1-diethoxy propane was nearly equal to the consumption of propionaldehyde (Fig. S.18b), resulting in carbon balance closure for C_3 compounds in the ethanol-propionaldehyde reaction on Sn-**CHA**-F-60. Ethanol conversions were ≤7% in all cases (Fig. S.18b), and the total concentrations of acetaldehyde, ethanol, and twice the 1,1-diethoxy propane concentration resulted in carbon balance closure for C_2 compounds. Closure of both C_2 and C_3 carbon balances demonstrates that further byproduct formation, other than 1,1-diethoxy propane, was not observed over Sn-**CHA** during intermolecular MPVO reactions of ethanol and propionaldehyde under the conditions studied here.

The initial 1-propanol formation rate measured on Sn-**CHA**-F-60 (Table 3) was 40× lower than that measured on Sn-Beta, but 60× higher than on Sn-xerogel. Rates were 90× higher on Sn-Beta-F-116 than on Sn-**CHA**-F-60 when normalized by the number of Sn sites in open coordination, which is the more reactive site in Sn-Beta predicted by theory[87,88] and identified by experiment for glucose isomerization mediated by an analogous intramolecular hydride shift.[40] The higher intermolecular MPVO reaction rates on Sn-Beta may reflect transport limitations in Sn-**CHA**, differences in prevalent coverages of reactive intermediates, or differences in transition state stability between the different frameworks. Isotopic tracer experiments using C_2D_5OH reactants were performed to confirm that 1-propanol products were formed over Sn-**CHA**-F-60 via a Lewis-acid mediated intermolecular hydride shift mechanism. The 1-propanol formed from reaction showed mass spectra with a one-unit increase in fragments for CH_3CH_2CHDOH (m/z = 60) and CHDOH (m/z = 32), as expected for deuterium incorporation within propionaldehyde (Section S.11, Fig. S.20).

3.3.2. Glucose-fructose isomerization via intramolecular MPVO cycles

Intramolecular MPVO cycles isomerize glucose into fructose via mechanisms whose details are generally accepted on Lewis acid sites incorporated within Beta zeolites, and were used to probe the reactivity of pyridine-accessible Sn sites in Sn-**CHA**. The catalytic cycle involves quasi-equilibrated adsorption, ring-opening and deprotonation of glucose at framework Sn sites, followed by a kinetically-relevant intramolecular 1,2-hydride shift step, and then by quasi-equilibrated fructose ring-closure and desorption.[93,94] First-order rate constants, measured in a kinetic regime in which adsorbed water molecules at framework metal centers are most abundant surface intermediates, are 10-50x higher (at 373 K) among low-defect than among high-defect Ti-Beta (per Ti site) and Sn-Beta (per open Sn site) zeolites.[40,95]

Table 2. Fraction of Lewis acidic Sn sites (mol per mol Sn) and SiOH densities (mol per g) on each sample quantified using different Lewis base titrants. Binding stoichiometries of one per Sn for each titrant.

Catalyst	Pyridine[a]	CD_3CN[b]				NH_3[c]
	Total	Total	Open	Closed	SiOH	Total
Sn-**CHA**-F-60	0.21	1.18	0.42	0.76	$5.26*10^{-4}$	1.08
Sn-**CHA**-F-70	0.20	1.14	0.36	0.78	$8.46*10^{-4}$	1.20
Sn-Beta-F-116	0.71	1.07	0.45	0.76	$5.71*10^{-5}$	0.77

[a]Errors are ± 20% [b]Errors are ± 20% [c]Errors are ± 5%

The higher first-order rate constants on low-defect M-Beta-F than high-defect M-Beta-OH zeolites reflect lower apparent free energies of activation, which measure the difference in stability between kinetically-relevant isomerization transition states and two water molecules bound at active metal sites.[40,95] As a result, glucose isomerization turnover rates and rate constants, measured in the first-order kinetic regime, provide a quantitative kinetic probe of the reactivity of Lewis acidic Sn sites, and can be used to assess the catalytic consequences of their primary local environment and secondary confining environment.

Glucose-fructose isomerization turnover rates (398 K, 1% (w/w) glucose; Table 3) on Sn-**CHA**-F-60, normalized by the number of pyridine-accessible Sn sites, were four orders-of-magnitude lower than turnover rates on Sn-Beta-F-116. Isomerization turnover rates were also four orders-of-magnitude lower on an amorphous Sn-xerogel, which contains only unconfined Sn sites, than on Sn-Beta-F-116 (Table 3). Isomerization turnover rates measured on Sn-xerogel and on Sn-**CHA**-F-60 were similar (within 2x), which is within the residual variation in turnover rates (within 2-3x) measured previously among Sn-Beta-F (>6 samples) or among Sn-Beta-OH (>16 samples) of varying Sn content.[40,73] The similar glucose-fructose isomerization turnover rates measured on Sn-xerogel and Sn-**CHA**, upon normalization by the number of pyridine-accessible sites, provides quantitative kinetic evidence supporting the presence of approximately 20% of the framework Sn sites located within mesoporous voids of Sn-**CHA**. These data highlight the crucial role of confining microporous environments in aqueous-phase glucose isomerization, and indicate that rates measured on Sn-Beta zeolites reflect reactions occurring at Sn sites confined within their 12-MR microporous voids, and not at any unconfined Sn sites that may be located at external crystallite surfaces. We conclude from these catalytic intramolecular and intermolecular MPVO probe reactions, together with the IR spectra collected after CD_3CN and pyridine titration, that Sn-**CHA** zeolites contain framework Sn sites that function as Lewis acids and are located within both microporous and mesoporous voids. Considering the single T-site present in the **CHA** framework, we next use this model, high-symmetry stannosilicate for calibrating experimental DNP NMR measurements using density functional theory.

3.4. Probing local Sn structure using ^{119}Sn DNP NMR spectroscopy

DNP enhanced $^{119}Sn\{^{1}H\}$ CPMAS NMR characterization of Sn-**CHA**-F-70 was performed in its hydrated and dehydrated states. An asymmetric peak characteristic of hexacoordinated Sn (ca. -720 ppm) was detected in the hydrated state (Fig. S.22a), while a broad peak characteristic of tetracoordinated Sn (ca. -430 ppm) was detected after dehydration (Fig. S.22b), with asymmetric broadening and a wider distribution of resonances reflecting the greater inhomogeneity or asymmetry of Sn sites after dehydration. The $^{119}Sn\{^{1}H\}$ CPMAS NMR sensitivity was considerably higher on the hydrated sample (ca. 1800 s signal averaging time for a spectrum with a signal-to-noise ratio = 35, Fig. S.22a), reflecting the proton-rich environment present within microporous voids, than on the dehydrated sample (ca. 21 h signal averaging time using Carr-Purcell Meiboom-Gill (CPMG)[96] echo trains for a spectrum with a signal-to-noise ratio = 15, Fig. S.22b), suggesting inefficient CP from ^{1}H to ^{119}Sn resulting from the absence of water (and perhaps TCE molecules from the biradical solution) within zeolitic pores. These changes in Sn coordination upon dehydration are consistent with XAS data (Section 3.1), and the behavior expected of framework Sn sites.

Table 3. Intramolecular and intermolecular MPVO reaction rates measured on the samples in this study.

Catalyst	Glucose isomerization rate (per total Sn)[a]	Glucose isomerization rate (per pyridine accessible Sn)[b]	Ethanol-propionaldehyde MPVO rate (per total Sn)[c]
Sn-**CHA**-F-60	$3.62*10^{-6}$	$1.72*10^{-5}$	$1.96*10^{-4}$
Sn-Beta-F-116	$2.90*10^{-1}$	$2.90*10^{-1}$	$8.24*10^{-3}$
Sn-xerogel	$7.45*10^{-6}$	$7.45*10^{-6}$	$3.48*10^{-6}$
Si-**CHA**-F	n. p.*	n.p.*	n. p.*

[a]398 K, 1% w/w glucose in water, Errors are ± 15%. [b]398 K, 1% w/w glucose in water, Errors are ± 15%. All Sn sites in Sn-Beta-F-116 and Sn-xerogel assumed to be pyridine accessible. [c]333 K, 0.6 M propionaldehyde in ethanol solvent, 1-propanol formation rate, Errors are ± 15%. *n. p., no products observed.

The increased NMR sensitivity afforded by DNP enables performing 2D $^{119}Sn\{^{1}H\}$ CP magic-angle turning (CPMAT) experiments, which can separate the chemical shift anisotropy (CSA) for each isotropic ^{119}Sn site that contributes to the broadened ^{119}Sn NMR resonance observed in the 1D spectra.[27] CSA is a second rank tensor defined by three principal components (δ_{11}, δ_{22}, and δ_{33}), and can also be described using the Herzfeld-Berger convention[97] by the isotropic chemical shift (δ_{iso}), span (Ω), and skew (κ) (Eqs. 2-4):

$$\delta_{iso} = \frac{1}{3}\left(\delta_{11} + \delta_{22} + \delta_{33}\right) \quad (2)$$

$$\Omega = \delta_{11} - \delta_{33} \quad (3)$$

$$\kappa = \frac{3(\delta_{22} - \delta_{iso})}{\Omega} \quad (4)$$

CSA is very sensitive to the neighboring electronic environment of the observed nuclei, and is thus an effective probe to elucidate Sn site structures at the molecular level.

The 2D $^{119}Sn\{^{1}H\}$ CPMAT NMR spectrum of the hydrated Sn-**CHA**-F-70 sample, which is shown in Figure 2, contained a single asymmetrically broadened peak on the isotropic dimension (δ_{iso} = -713 ppm) and did not contain a sharp feature for extraframework SnO_2 (-605 ppm).[71] The corresponding projection (at δ_{iso}) on the isotropic dimension was extracted and fit to acquire the experimental CSA parameters listed in Table 4. Two components with the same isotropic chemical shift, but different span (Ω) and skew (κ), were required to fit the experimental data, a surprising result considering the single T-site in the **CHA** framework (Figs. 2a and S.22c). This two-component fitting suggests at least two similar Sn sites are present, with slightly different coordination environments or local geometries, but coincidentally at the same isotropic chemical shift. These CSA components do not reflect contributions of Sn sites incorporated in minority amorphous stannosilicate domains, which are characterized by different isotropic chemical shifts (δ_{iso} = -600, -626, and -690 ppm, Fig. S.23). 2D $^{119}Sn\{^{1}H\}$ CPMAT experiments performed with varying DNP build-up time (1-20 s recycle delays), did not affect the relative areas of the two component peaks used in the CSA fitting (Section S.12, Table S.4), indicating that both sites are distributed evenly within the sample and unaffected by ^{1}H-^{1}H spin diffusion on the time scale studied. Overall, these data suggest that these two components represent Sn sites of different local structure incorporated within the **CHA** framework and evenly distributed among mesoporous and microporous voids.

Table 4. Chemical shift anisotropy (CSA) parameters for the two different Sn sites identified in the hydrated and dehydrated states of Sn-**CHA**-F-70.

Catalyst	CSA Parameters		
	chemical shift (δ_{iso}, ppm)[a]	Span (Ω, ppm)[b]	skew (κ)[b]
Hydrated Sn-**CHA**			
Site 1	-713 ± 3	139 ± 4	0.05 ± 0.06
Site 2	-712 ± 3	56 ± 4	-0.25 ± 0.25
Dehydrated Sn-**CHA**			
Site 3	-442 ± 9	159 ± 12	0.24 ± 0.08
Site 4	-484 ± 10	139 ± 14	0.16 ± 0.11

[a]Errors are determined by peak width

[b]Errors are the results of error propagation calculations

The 2D $^{119}Sn\{^{1}H\}$ CPMAT NMR spectrum of dehydrated Sn-**CHA**-F-70 showed two asymmetrically broadened resonances on the isotropic dimension (δ_{iso} = -437 and -480 ppm, fit from the 1D DNP enhanced CP-Total Sideband Suppression spectrum), which were analyzed to acquire experimental CSA parameters (Section S.12, Fig. S.24). The resonance at -480 ppm

appears between the range of chemical shifts characteristic of tetracoordinated (ca. -430 ppm) and pentacoordinated Sn (ca. -550 ppm), but was too low in intensity to estimate CSA parameters (Table 4). The Sn site at -480 ppm may represent a minor fraction of Sn that is not completely dehydrated in Sn-**CHA**-F-70 despite vacuum treatment (773 K), which might reflect strongly adsorbed water molecules bound at silanol and stannanol groups in defect Sn sites (Scheme 1). The CSA parameters for the resonance at -437 ppm are similar to those reported previously for dehydrated Sn-Beta, although the larger span for Sn-**CHA** (159 ppm) than for Sn-Beta (ca. 100 ppm)[27] may reflect more distorted local Sn environments in **CHA** (Table 4).

Dehydrated Sn-**CHA**-F-70 was saturated with ^{15}N-pyridine at ambient temperature and characterized by ^{15}N and ^{119}Sn DNP NMR to further probe the structure of Sn sites that bind pyridine. The 1D ^{119}Sn{^{1}H} CPMAS NMR spectrum of ^{15}N-pyridine-saturated Sn-**CHA**-F-70 (Fig. S.28) shows a broad distribution of resonances ranging from -400 to -750 ppm, while the 2D ^{119}Sn{^{1}H} CPMAT NMR spectrum (Fig. S.29) shows two peaks in the isotropic dimension characteristic of pentacoordinated (ca. -596 ppm) and hexacoordinated Sn (ca. -694 ppm), whose corresponding CSA parameters are listed in Table 5. The pentacoordinated Sn resonance was expected from the equimolar binding of pyridine to Sn,[40] while the hexacoordinated Sn resonance implies that some Sn sites can bind a second pyridine molecule. The binding of two pyridine molecules at a single Sn site, which was not observed by IR spectroscopy (423 K), likely resulted from the excess ^{15}N pyridine used to saturate Sn-**CHA** at ambient temperature prior to NMR experiments.

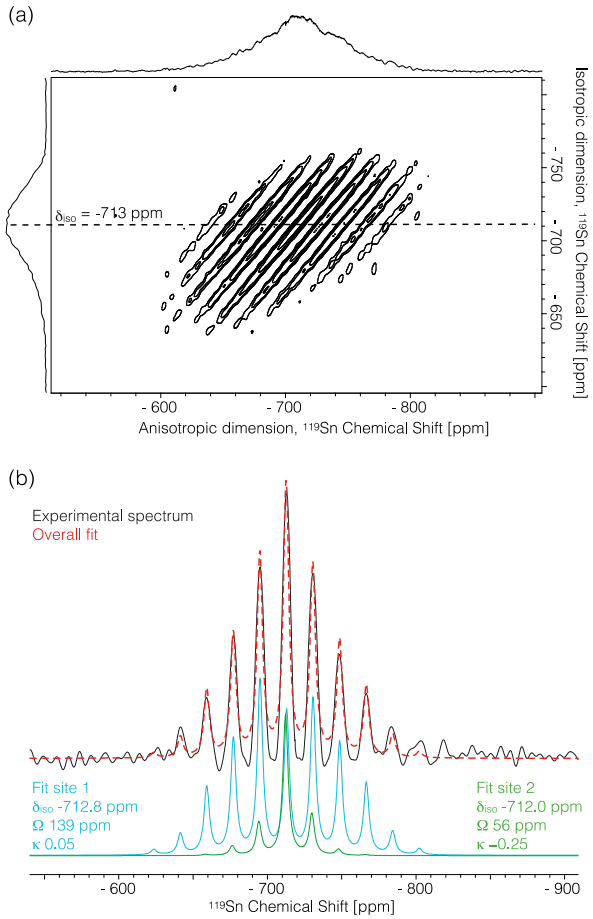

Figure 2. (a) 2D ^{119}Sn CPMAT spectrum of hydrated Sn-**CHA**-F-70 and (b) extracted 1D ^{119}Sn NMR spectrum for Sn-**CHA**-F-70 (blue trace) fit with two sets of CSA parameters (light blue and green traces) and their combination (red trace) resulting in better description of the experimental spectrum. The spectrum was acquired on Bruker 600 MHz (14.1 T) DNP NMR spectrometer. MAS = 4 kHz; CP contact time = 1.5 ms; recyle delay = 3.5 s; 256 scans per *t1* increment, and 85 *t1* increments were acquired. The CSA fit was done using solid lineshape feature in Bruker's topspin program.

Two isotropic peaks were observed in the 1D DNP enhanced ^{15}N{^{1}H} CPMAS NMR spectrum of ^{15}N-pyridine saturated Sn-**CHA**-F-70 (Fig. S.30), and the 2D ^{15}N CPMAT NMR is shown in Figure 3, with the associated CSA parameters given in Table 5. The resonance at 262 ppm reflects pyridine bound to Lewis acidic Sn sites, similar to that observed for stannosilicate materials with pores large enough to accommodate pyridine (MFI, MCM-41, Beta, xerogel, Fig. S.31).[98] The resonance centered at 289 ppm reflects pyridine interacting with silanol groups,[98] an assignment corroborated by the ^{15}N{^{1}H} CPMAS NMR spectrum of ^{15}N-pyridine saturated Si-**CHA**-F (δ_{iso} = 286 ppm, Section S.13, Fig. S.32). Among the metallosilicates studied by Gunther et al., only high-defect zeolites synthesized in alkaline media showed a ^{15}N resonance for pyridine bound to SiOH groups.[98] Thus, the observation of this resonance in Sn-**CHA**-F-70 reflects the presence of a considerable concentration of silanol defects, consistent with H_2O adsorption isotherms that quantified 12× higher H_2O uptake in Sn-**CHA**-F-70 than in Sn-Beta-F,[40] and with CD_3CN titration that quantified 2-12× higher SiOH concentrations in Sn-**CHA** than in Sn-Beta-F (Table 2).[40] The presence of these defects is also consistent with the high percentage of (HO)-Si-$(OSi)_3$ (Q_3) sites (21%) quantified by direct-polarized ^{29}Si solid-state NMR spectrum (Fig. S.27). Taken together, the IR and NMR data for pyridine-saturated Sn-**CHA** zeolites indicate that ca. 20% of its framework Sn sites are located within mesoporous voids that also contain a high concentration of SiOH defects.

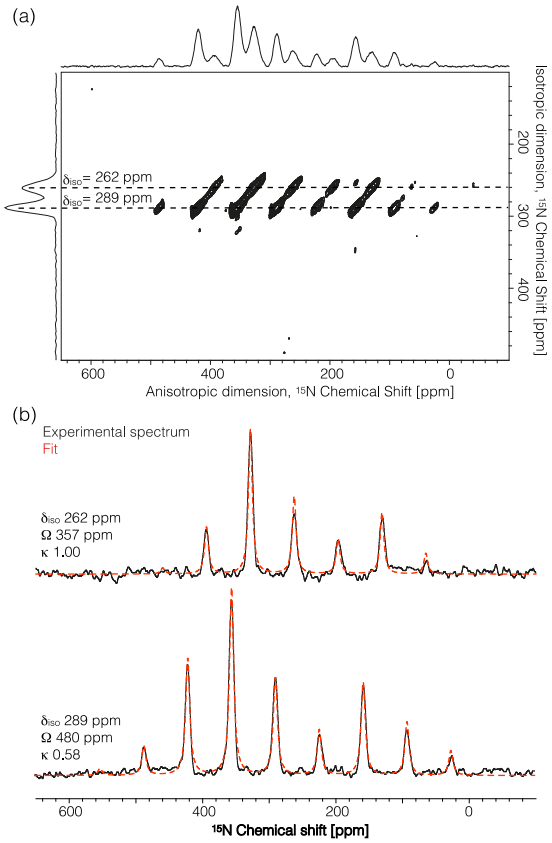

Figure 3. (a) 2D $^{15}N\{^{1}H\}$ CPMAT NMR spectrum and (b) extracted 1D ^{15}N NMR spectra and corresponding CSA fit for pyridine-saturated Sn-**CHA**-F-70. The spectrum was acquired on Bruker 600 MHz (14.1 T) DNP NMR spectrometer. MAS= 4 kHz; CP contact time= 8.0 ms; recyle delay = 4.5 s; 112 scans per *t1* increment, and 112 *t1* increments were acquired. The CSA fit was performed using the solid lineshape feature in Bruker's Topspin program.

3.5. DFT calculations of ^{119}Sn DNP NMR chemical shifts, spans, and CSA parameters

The different local structures of Sn sites proposed to be present in zeolitic frameworks, which are closed, hydrolyzed-open, and defect sites (Scheme 1), were investigated by DFT calculations, with optimized structures for Sn-**CHA** shown in Figure 4. The hydrated states of Sn sites (pseudo-octahedral geometry) were modeled with two water molecules bound to Sn for closed and defect sites, and one water molecule bound to Sn for the hydrolyzed-open site given its additional bond to the proximal silanol group. Two additional water molecules outside the Sn coordination sphere and implicit water (dielectric constant, ,ε, set to 80.4) were also included in the model (Fig. 4).

Table 5. Chemical shift anisotropy (CSA) parameters for pyridine-saturated, dehydrated Sn-**CHA**-F-70 and Si-**CHA**-F.

Catalyst	Detected Nuclei	CSA Parameters: Chemical (δ_{iso}, ppm)	shiftspan (Ω, ppm)	skew (κ)
Sn-**CHA**-F-70				
Lewis acidic Sn sites	^{15}N	262 ± 5	357 ± 7	1.00 ± 0.06
One pyridine	^{119}Sn	-596 ± 5	331 ± 7	-0.32 ± 0.06
Two pyridine	^{119}Sn	-694 ± 6	132 ± 8	0.18 ± 0.18
SiOH groups	^{15}N	289 ± 5	480 ± 7	0.58 ± 0.04
Si-**CHA**-F	^{15}N	286 ± 10	--	--

DFT-optimized structures of hydrated closed and defect Sn sites have average Sn-O distances of 2.04 Å, and the hydrolyzed-open Sn site has an average Sn-O distance of 2.02 Å. All values are similar to the average Sn-O bond distances for hydrated Sn-**CHA** measured by XAS (2.01 ± 0.02 Å, Section S.8). Calculated ^{119}Sn NMR CSA parameters for hydrated defect and hydrolyzed-open sites (Section S.14, Table S.5) provided closest agreement to the two sets of CSA parameters required to fit the experimental data. Given the peak width of the NMR resonances (6 ppm) and the error between calculated and experimental values (± 10 ppm), it is not possible to distinguish hydrolyzed-open and defect sites from the isotropic peak. Moreover, the difference between the DFT calculated spans for hydrated hydrolyzed-open and defect Sn sites (74 ppm) resembles the difference in the spans of the two components required to fit the experimental ^{119}Sn DNP NMR data for hydrated Sn-**CHA** (ca. 83 ppm). Therefore, we conclude that the two components identified in 2D $^{119}Sn\{^{1}H\}$ CPMAT NMR spectra reflect hydrated hydrolyzed-open and defect framework Sn sites. We note, however, that experimental DNP NMR measurements may enhance contributions from ^{119}Sn sites in close proximity with protons due to more efficient polarization transfer, as observed in the increased sensitivity to $(HO)_2Si(OSi)_2$ (Q_2) and Q_3 silanol groups in ^{29}Si DNP NMR (Figs. S.25-S.26) compared to direct-excitation ^{29}Si NMR (Fig. S.27).

DFT-optimized structures of dehydrated hydrolyzed-open Sn sites showed average Sn-O distances of 1.98 Å, similar to the average Sn-O bond distance measured for dehydrated Sn-**CHA** by XAS (1.96 ± 0.02 Å, Section S.8). The DFT-optimized structure was a pentacoordinate Sn site, while the average coordination number from XAS was four. Furthermore, the calculated ^{119}Sn NMR parameters for hydrolyzed-open Sn sites (-566 ppm, Table S.5) did not agree with those measured experimentally (-437 and -480 ppm). Closed and defect Sn sites showed average Sn-O distances of 1.88 Å,

which are significantly lower than the Sn-O bond distance in dehydrated Sn-**CHA** measured by XAS (1.96 ± 0.02 Å) and may reflect incomplete dehydration of Sn-**CHA** prior to XAS measurements. Calculated ^{119}Sn NMR parameters of dehydrated defect Sn sites were indistinguishable from dehydrated closed Sn sites (Fig. 4; Table S.5), in contrast to calculated ^{119}Sn NMR chemical shifts of Sn-Beta[27] which are separated by ca. 20 ppm for defect and closed sites.

The similar isotropic chemical shifts for both sites appear to reflect strong hydrogen bonding between SiOH and SnOH groups in defect Sn sites that are present in close proximity in the **CHA** framework. Calculated NMR parameters for pyridine-saturated Sn-CHA (^{119}Sn and ^{15}N) suggest that the pentacoordinate Sn sites observed experimentally reflect one pyridine molecule coordinated to closed Sn sites, while two pyridine molecules most likely coordinate to defect Sn sites and result in hexacoordinated Sn (Fig. 4; Table S.6). These structural assignments of the different pyridine binding modes to Sn sites are also consistent with the calculated pyridine adsorption energies (Table S.7), which further indicate that closed and defect Sn sites favor binding of one and two pyridine molecules, respectively, at 298 K.

In summary, comparison of the experimental and calculated ^{119}Sn NMR parameters suggests that the Sn sites observed in hydrated Sn-**CHA** are predominantly defect and hydrolyzed-open Sn sites, whose signals may be preferentially enhanced by DNP due to their proton-rich environment, while those observed in dehydrated Sn-**CHA** are predominantly defect and closed Sn sites, which cannot be distinguished by NMR. The high ratio of Si Q_3 sites in direct-polarized ^{29}Si NMR (21%, Fig. S.27) also suggests that silanol defects are present in large concentrations on Sn-**CHA**-F zeolites prepared using the methods here, and likely located within mesoporous voids. In pyridine-titrated dehydrated Sn-**CHA**, polarization transfer from protons within coordinated pyridine can enhance the ^{119}Sn NMR signal, and the different binding stoichiometries of pyridine molecules (one or two) results in Sn sites with different coordination numbers (five or six, respectively), such that both closed and defect sites can be detected and distinguished. These assignments also suggest that closed sites present after sample dehydration under vacuum can undergo reversible structural changes to form hydrolyzed-open sites upon hydration.

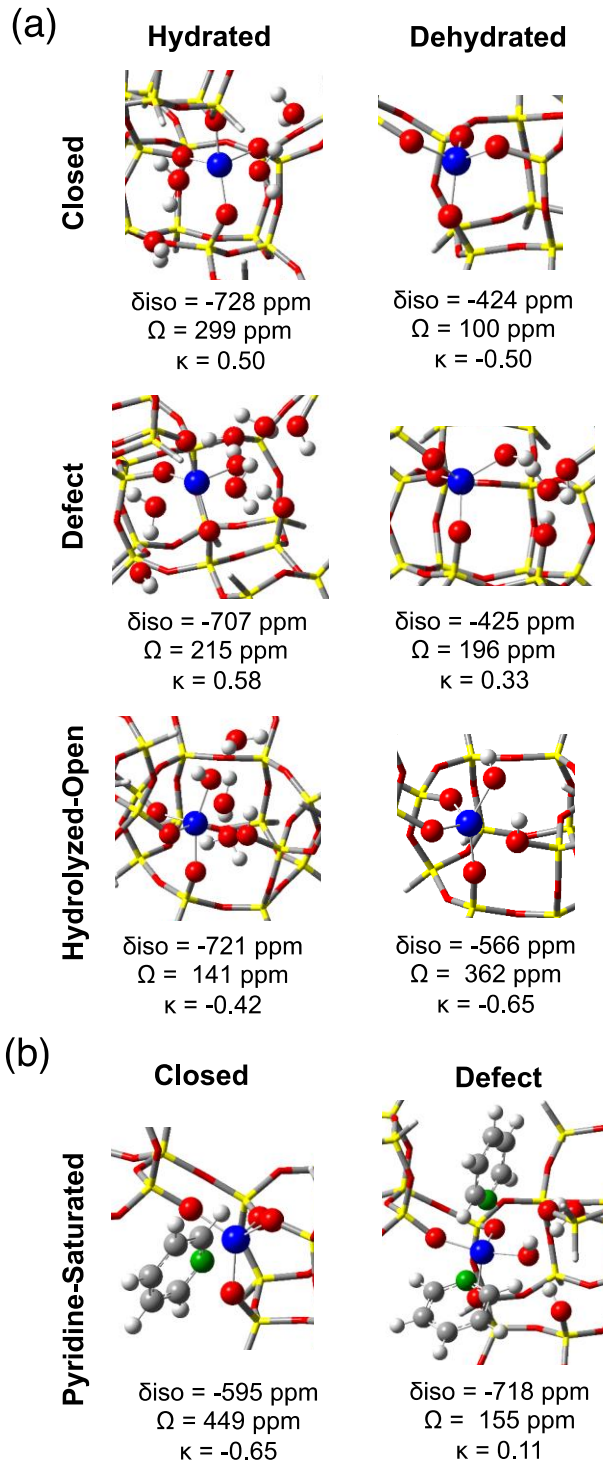

Figure 4. DFT optimized structures for (a) hydrated closed Sn sites, defect-open Sn sites, and hydrolyzed-open Sn sites, for dehydrated closed Sn sites, defect Sn sites, and hydrolyzed-open Sn sites, and (b) for pyridine saturated closed Sn, and defect Sn sites. Calculated isotropic chemical shifts (δ_{iso}), span (Ω), and skew (κ) are shown for each site. Details of DFT calculations are in supporting information, Section S.14.

4. Conclusions

Chabazite molecular sieves containing isomorphously substituted framework tin heteroatoms (Sn-**CHA**) were prepared via direct fluoride-mediated hydrothermal synthesis routes. Lewis

acidic Sn sites in Sn-**CHA** were titrated in equimolar stoichiometry by ammonia and d_3-acetonitrile, providing values identical within experimental error to the total Sn content. These data indicate that integrated molar extinction coefficients for IR vibrations of CD_3CN bound at Sn sites in Sn-Beta can be used to quantify such sites in Sn-**CHA**. IR spectra of Sn-**CHA** zeolites titrated by pyridine, a molecule too large to traverse eight-membered ring **CHA** windows, indicated that 20% of the framework Sn sites were located within disordered mesoporous voids.

Sn-**CHA** zeolites catalyze intermolecular MPVO and subsequent condensation reactions of ethanol and propionaldehyde, confirming that framework Sn sites confined within **CHA** micropores function as Lewis acid centers capable of mediating hydride shift steps. In contrast, aqueous-phase glucose-fructose isomerization at Sn sites located within mesoporous voids of Sn-**CHA** and amorphous silica matrices proceeds at turnover rates that are four orders-of-magnitude lower than Sn sites confined within Sn-Beta zeolites. These data provide evidence that unconfined Sn sites in stannosilicates are effectively unreactive for aqueous-phase glucose isomerization.

DNP NMR characterizations of Sn-**CHA** zeolites show that Sn sites were incorporated into framework lattice positions, consistent with UV-Visible and X-ray absorption spectra that detect tetracoordinated Sn centers upon sample dehydration. The NMR signal enhancements enabled by DNP allow resolving two distinct Sn sites characterized by identical isotropic chemical shift but different chemical shift anisotropy. Comparison of experimentally measured ^{119}Sn NMR CSA parameters with those calculated from DFT supports the presence of framework Sn sites with (defect) and without (closed) neighboring framework Si vacancy defects in dehydrated Sn-**CHA**, which form hydrated defect and hydrolyzed-open sites upon exposure to ambient conditions or aqueous solution. Such assignments to Sn sites in different local coordination environments (e.g., defect, hydrolyzed-open, closed) were made possible by the structural simplicity of the **CHA** framework, which contains one lattice T-site and facilitates more accurate theoretical modeling of experimental spectra. Overall, integrating the controlled synthesis of a model crystalline catalyst containing isolated metal centers, the detection of specific spectroscopic signatures sensitive to their primary coordination and secondary confining environments, and the computation of plausible active site structures, was essential to resolve the local structure of metal binding sites and to demonstrate the role of secondary confining voids in catalysis.

Supporting Information. Statement of author contributions, X-ray diffraction patterns, scanning electron micrographs, adsorption isotherms and pore size distributions, transmission electron micrographs, diffuse reflectance UV-visible spectra and Tauc plots, thermogravimetric analysis, X-ray absorption spectra, supplementary infrared spectra, ammonia temperature programmed desorption, intermolecular MPVO reactions, additional details for NMR spectra, supplementary NMR spectra, DFT calculations

AUTHOR INFORMATION

Corresponding Author

*E-mail: ccoperet@ethz.ch, rgounder@purdue.edu

Present Addresses

†Present address: Department of Chemistry and Biochemistry, University of California Los Angeles, Los Angeles, CA 90095

Author Contributions

The manuscript was written through contributions of all authors. All authors have given approval to the final version of the manuscript. ‡J. W. H. and W.-C. L. contributed equally to the work.

Notes

The authors declare no competing financial interest.

ACKNOWLEDGMENTS

Purdue researchers acknowledge the financial support provided by the Purdue Process Safety and Assurance Center (P2SAC) and a 3M Non-Tenured Faculty Grant. At Purdue, we thank Juan Carlos Vega-Vila for assistance with glucose isomerization reactions, Evan Wegener and Dr. Jeffrey T. Miller for XAS measurements and data analysis, Jason Bates for measurement of H_2O adsorption isotherms, and Michael Cordon for assistance with SEM imaging. We also thank Sachem, Inc. for supplying the organic structure-directing agent used in synthesis of **CHA** molecular sieves. The work of WCL and ACV is supported by Swiss National Foundation (200020_149704 and Ambizione project PZ00P2_148059, respectively). ACV also acknowledges the Holcim Stiftung for financial support. WCL thanks Mr. Erwin Lam for the help and discussion about DFT calculations. We thank Dr. David Gajan and Dr. Anne Lesage at CRMN Lyon for assisting with measurements on the 400 MHz DNP spectrometer and for fruitful discussions. We thank Prof. Lyndon Emsley and the group members at EPFL for fruitful discussions. We also thank ScopeM (ETH-Zürich) for use of their electron microscopy facilities and Dr. Frank Krumeich for recording TEM images.

REFERENCES

(1) Pelletier, J. D. A.; Basset, J. M. Catalysis by Design: Well-Defined Single-Site Heterogeneous Catalysts. *Acc. Chem. Res.* **2016,** *49*, 664-677.

(2) Copéret, C.; Comas-Vives, A.; Conley, M. P.; Estes, D. P.; Fedorov, A.; Mougel, V.; Nagae, H.; Nunez-Zarur, F.; Zhizhko, P. A. Surface Organometallic and Coordination Chemistry Toward Single-Site Heterogeneous Catalysts: Strategies, Methods, Structures, and Activities. *Chem. Rev.* **2016,** *116*, 323-421.

(3) Thomas, J. M. The Societal Significance of Catalysis and the Growing Practical Importance of Single-site Heterogeneous Catalysts. *Proc. R. Soc. A* **2012,** *468*, 1884-1903.

(4) Guzman, J.; Gates, B. C. Supported Molecular Catalysts: Metal Complexes and Clusters on Oxides and Zeolites. *Dalton Trans.* **2003**, 0, 3303-3318.

(5) Stalzer, M. M.; Delferro, M.; Marks, T. J. Supported Single-Site Organometallic Catalysts for the Synthesis of High-Performance Polyolefins. *Catal. Lett.* **2015,** *145*, 3-14.

(6) Notestein, J. M.; Iglesia, E.; Katz, A. Grafted Metallocalixarenes as Single-site Surface Organometallic Catalysts. *J. Am. Chem. Soc.* **2004,** *126*, 16478-16486.

(7) Wegener, S. L.; Marks, T. J.; Stair, P. C. Design Strategies for the Molecular Level Synthesis of Supported Catalysts. *Acc. Chem. Res.* **2012,** *4*5, 206-214.

(8) Pucino, M.; Mougel, V.; Schowner, R.; Fedorov, A.; Buchmeiser, M. R.; Copéret, C. Cationic Silica-Supported N-Heterocyclic Carbene Tungsten Oxo Alkylidene Sites: Highly Active and Stable Catalysts for Olefin Metathesis. *Angew. Chem., Int. Ed.* **2016,** *55*, 4300-4302.

(9) Bhan, A.; Allian, A. D.; Sunley, G. J.; Law, D. J.; Iglesia, E. Specificity of Sites Within Eight-membered Ring Zeolite Channels for Carbonylation of Methyls to Acetyls. *J. Am. Chem. Soc.* **2007***,* *129*, 4919-2924.

(10) Gounder, R.; Iglesia, E. The Catalytic Diversity of Zeolites: Confinement and Solvation Effects Within Voids of Molecular Dimensions. *Chem. Commun.* **2013,** *49*, 3491-3509.
(11) Šepa, J.; Lee, C.; Gorte, R. J.; White, D.; Kassab, E.; Evleth, E. M.; Jessri, H.; Allavena, M. Carbonyl C-13 Shielding Tensors and Heats of Adsorption of Acetone Adsorbed in Silicalite and the 1:1 Stoichiometric Complex in H-ZSM-5. *J. Phys. Chem.* **1996,** *100*, 18515-18523.
(12) Gorte, R. J.; White, D. Measuring Sorption Effects at Zeolite Acid Sites: Pursuing Ideas from W.O. Haag. *Microporous Mesoporous Mater.* **2000,** *35-36*, 447-455.
(13) Davis, M. E. New Vistas in Zeolite and Molecular-Sieve Catalysis. *Acc. Chem. Res.* **1993,** *26*, 111-115.
(14) Corma, A. Inorganic Solid Acids and Their Use in Acid-Catalyzed Hydrocarbon Reactions. *Chem. Rev.* **1995,** *95*, 559-614.
(15) Corma, A.; Nemeth, L. T.; Renz, M.; Valencia, S. Sn-zeolite Beta as a Heterogeneous Chemoselective Catalyst for Baeyer-Villiger Oxidations. *Nature* **2001,** *412*, 423-425.
(16) Corma, A.; Domine, M. E.; Nemeth, L.; Valencia, S. AI-free Sn-beta Zeolite as a Catalyst for the Selective Reduction of Carbonyl Compounds (Meerwein-Ponndorf-Verley Reaction). *J. Am. Chem. Soc.* **2002,** *124*, 3194-3195.
(17) Moliner, M.; Román-Leshkov, Y.; Davis, M. E. Tin-containing Zeolites are Highly Active Catalysts for the Isomerization of Glucose in Water. *Proc. Natl. Acad. Sci. USA* **2010,** *107*, 6164-6168.
(18) Bermejo-Deval, R.; Orazov, M.; Gounder, R.; Hwang, S. J.; Davis, M. E. Active Sites in Sn-Beta for Glucose Isomerization to Fructose and Epimerization to Mannose. *ACS Catal.* **2014,** *4*, 2288-2297.
(19) Boronat, M.; Concepción, P.; Corma, A.; Renz, M.; Valencia, S. Determination of the Catalytically Active Oxidation Lewis Acid Sites in Sn- beta Zeolites, and Their Optimisation by the Combination of Theoretical and Experimental Studies. *J. Catal.* **2005,** *234*, 111-118.
(20) Wolf, P.; Valla, M.; Rossini, A. J.; Comas-Vives, A.; Nunez-Zarur, F.; Malaman, B.; Lesage, A.; Emsley, L.; Copéret, C.; Hermans, I. NMR Signatures of the Active Sites in Sn-beta Zeolite. *Angew. Chem., Int. Ed.* **2014,** *53*, 10179-10183.
(21) Can, T. V.; Ni, Q. Z.; Griffin, R. G. Mechanisms of Dynamic Nuclear Polarization in Insulating Solids. *J. Magn. Reson.* **2015,** *253*, 23-35.
(22) Rossini, A. J.; Zagdoun, A.; Lelli, M.; Lesage, A.; Copéret, C.; Emsley, L. Dynamic Nuclear Polarization Surface Enhanced NMR Spectroscopy. *Acc. Chem. Res.* **2013,** *46*, 1942-1951.
(23) Barnes, A. B.; De Päepe, G.; van der Wel, P. C. A.; Hu, K. N.; Joo, C. G.; Bajaj, V. S.; Mak-Jurkauskas, M. L.; Sirigiri, J. R.; Herzfeld, J.; Temkin, R. J.; Griffin, R.G. High-field Dynamic Nuclear Polarization for Solid and Solution Biological NMR. *Appl. Magn. Reson.* **2008,** *34*, 237-263.
(24) Kobayashi, T.; Lafon, O.; Thankamony, A. S. L.; Slowing, II; Kandel, K.; Carnevale, D.; Vitzthum, V.; Vezin, H.; Amoureux, J. P.; Bodenhausen, G.; Pruski, M. Analysis of Sensitivity Enhancement by Dynamic Nuclear Polarization in Solid-state NMR: a Case Study of Functionalized Mesoporous Materials. *Phys. Chem. Chem. Phys.* **2013,** *15*, 5553-5562.
(25) Gunther, W. R.; Michaelis, V. K.; Caporini, M. A.; Griffin, R. G.; Román-Leshkov, Y. Dynamic Nuclear Polarization NMR Enables the Analysis of Sn-Beta Zeolite Prepared with Natural Abundance Sn-119 Precursors. *J. Am. Chem. Soc.* **2014,** *136*, 6219-6222.
(26) Lafon, O.; Rosay, M.; Aussenac, F.; Lu, X. Y.; Trebosc, J.; Cristini, O.; Kinowski, C.; Touati, N.; Vezin, H.; Amoureux, J. P. Beyond the Silica Surface by Direct Silicon-29 Dynamic Nuclear Polarization. *Angew. Chem., Int. Ed.* **2011,** *50*, 8367-8370.
(27) Wolf, P.; Valla, M.; Nunez-Zarur, F.; Comas-Vives, A.; Rossini, A. J.; Firth, C.; Kallas, H.; Lesage, A.; Emsley, L.; Copéret, C.et al. Correlating Synthetic Methods, Morphology, Atomic-Level Structure, and Catalytic Activity of Sn-beta Catalysts. *ACS Catal.* **2016,** *6*, 4047-4063.
(28) Bare, S. R.; Kelly, S. D.; Sinkler, W.; Low, J. J.; Modica, F. S.; Valencia, S.; Corma, A.; Nemeth, L. T. Uniform Catalytic Site in Sn-beta-zeolite Determined Using X-ray Absorption Fine Structure. *J. Am. Chem. Soc.* **2005,** *127*, 12924-12932.
(29) Newsam, J. M.; Treacy, M. M. J.; Koetsier, W. T.; Degruyter, C. B. Structural Characterization of Zeolite-Beta. *Proc. R. Soc. A* **1988,** *420*, 375-405.
(30) Tolborg, S.; Katerinopoulou, A.; Falcone, D. D.; Sadaba, I.; Osmundsen, C. M.; Davis, R. J.; Taarning, E.; Fristrup, P.; Holm, M. S. Incorporation of Tin Affects Crystallization, Morphology, and Crystal Composition of Sn-Beta. *J. Mater. Chem. A* **2014,** *2*, 20252-20262.
(31) Zicovich-Wilson, C. M.; Dovesi, R. Titanium-containing Zeolites. A Periodic Ab Initio Hartree-Fock Characterization. *J. Phys. Chem. B* **1998,** *102*, 1411-1417.
(32) Damin, A.; Bordiga, S.; Zecchina, A.; Doll, K.; Lamberti, C. Titchabazite as a Model System of Ti(IV) in Ti-zeolites: A Periodic Approach. *J. Chem. Phys.* **2003,** *118*, 10183-10194.
(33) Han, L. N.; Wen, C.; Wu, Z. P.; Wang, J. C.; Chang, L. P.; Feng, G.; Zhang, R. B.; Kong, D. J.; Liu, J. W. Density Functional Theory Investigations into the Structures and Acidity Properties of Ti-doped SSZ-13 Zeolite. *Microporous Mesoporous Mater.* **2017,** *237*, 132-139.
(34) Zicovich-Wilson, C. M.; Dovesi, R.; Corma, A. Interaction of Ti-zeolites with Water. A Periodic Ab Initio Study. *J. Phys. Chem. B* **1999,** *103*, 988-994.
(35) Wen, C.; Geng, L.; Han, L. N.; Wang, J. C.; Chang, L. P.; Feng, G.; Kong, D. J.; Liu, J. W. A Comparative First Principles Study on Trivalent Ion Incorporated SSZ-13 Zeolites. *Phys. Chem. Chem. Phys.* **2015,** *17*, 29586-29596.
(36) Wang, C. M.; Brogaard, R. Y.; Weckhuysen, B. M.; Norskov, J. K.; Studt, F. Reactivity Descriptor in Solid Acid Catalysis: Predicting Turnover Frequencies for Propene Methylation in Zeotypes. *J. Phys. Chem. Lett.* **2014,** *5*, 1516-1521.
(37) Bukowski, B. C.; Greeley, J. Scaling Relationships for Molecular Adsorption and Dissociation in Lewis Acid Zeolites. *J. Phys. Chem. C* **2016,** *120*, 6714-6722.
(38) Eilertsen, E. A.; Bordiga, S.; Lamberti, C.; Damin, A.; Bonino, F.; Arstad, B.; Svelle, S.; Olsbye, U.; Lillerud, K. P. Synthesis of Titanium Chabazite: A New Shape Selective Oxidation Catalyst with Small Pore Openings and Application in the Production of Methyl Formate from Methanol. *Chemcatchem* **2011,** *3*, 1869-1871.
(39) Diaz-Cabanas, M. J.; Barrett, P. A. Synthesis and Structure of Pure SiO2 Chabazite: the SiO2 Polymorph with the Lowest Framework Density. *Chem. Commun.* **1998**, 0, 1881-1882.
(40) Harris, J. W.; Cordon, M. J.; Di Iorio, J. R.; Vega-Vila, J. C.; Ribeiro, F. H.; Gounder, R. Titration and Quantification of Open and Closed Lewis Acid Sites in Sn-Beta Zeolites that Catalyze Glucose Isomerization. *J. Catal.* **2016,** *335*, 141-154.
(41) van Grieken, R.; Martos, C.; Sanchez-Sanchez, M.; Serrano, D. P.; Melero, J. A.; Iglesias, J.; Cubero, A. G. Synthesis of Sn-silicalite from Hydrothermal Conversion of SiO2-SnO2 Xerogels. *Microporous Mesoporous Mater.* 2009, *119*, 176-185.
(42) Cybulskis, V. J.; Harris, J. W.; Zvinevich, Y.; Ribeiro, F. H.; Gounder, R. A Transmission Infrared Cell Design for Temperature-controlled Adsorption and Reactivity Studies on Heterogeneous Catalysts. *Rev. Sci. Inst.* **2016,** *87*, 103101.
(43) Bates, S. A.; Delgass, W. N.; Ribeiro, F. H.; Miller, J. T.; Gounder, R. Methods for NH3 Titration of Bronsted Acid Sites in Cu-zeolites that Catalyze the Selective Catalytic Reduction of NOx with NH3. *J. Catal.* **2014,** *312*, 26-36.
(44) Zagdoun, A.; Casano, G.; Ouari, O.; Schwarzwalder, M.; Rossini, A. J.; Aussenac, F.; Yulikov, M.; Jeschke, G.; Coperet, C.; Lesage, A.; Tordo, P.; Emsley, L. Large Molecular Weight Nitroxide Biradicals Providing Efficient Dynamic Nuclear Polarization at Temperatures up to 200 K. *J. Am. Chem. Soc.* **2013,** *135*, 12790-12797.
(45) Zagdoun, A.; Rossini, A. J.; Gajan, D.; Bourdolle, A.; Ouari, O.; Rosay, M.; Maas, W. E.; Tordo, P.; Lelli, M.; Emsley, L.; Lesage, A.; Copéret, C. Non-aqueous Solvents for DNP Surface

Enhanced NMR Spectroscopy. *Chem. Commun.* **2012,** *48*, 654-656.
(46) Hu, J. Z.; Alderman, D. W.; Ye, C. H.; Pugmire, R. J.; Grant, D. M. An Isotropic Chemical Shift-Chemical Shift Anisotropy Magic-Angle Slow-Spinning 2D NMR Experiment. *J. Magn. Reson. Ser. A* **1993,** *105*, 82-87.
(47) Vosko, S. H.; Wilk, L.; Nusair, M. Accurate Spin-Dependent Electron Liquid Correlation Energies for Local Spin-density Calculations - A Critical Analysis. *Can. J. Phys.* **1980,** *58*, 1200-1211.
(48) Lee, C. T.; Yang, W. T.; Parr, R. G. Development of the Colle-Salvetti Correlation-Energy Formula into a Functional of the Electron-Density. *Phys. Rev. B* **1988,** *37*, 785-789.
(49) Becke, A. D. Density-functional Thermochemistry. III. The Role of Exact Exchange. *J. Chem. Phys.* **1993,** *98*, 5648-5652.
(50) Stephens, P. J.; Devlin, F. J.; Chabalowski, C. F.; Frisch, M. J. Ab-initio Calculation of Vibrational Absorption and Circular-dichroism Spectra Using Density-Functional Force-fields *J. Phys. Chem.* **1994,** *98*, 11623-11627.
(51) Grimme, S.; Antony, J.; Ehrlich, S.; Krieg, H. A Consistent and Accurate Ab Initio Parametrization of Density Functional Dispersion Correction (DFT-D) for the 94 Elements H-Pu. *J. Chem. Phys.* **2010,** *132*, 154104.
(52) Grimme, S.; Ehrlich, S.; Goerigk, L. Effect of the Damping Function in Dispersion Corrected Density Functional Theory. *J. Comput. Chem.* **2011,** *32*, 1456-1465.
(53) M. J. Frisch; G. W. Trucks; H. B. Schlegel; G. E. Scuseria; M. A. Robb; J. R. Cheeseman; G. Scalmani; V. Barone; G. A. Petersson; H. Nakatsuji; X. Li; M. Caricato; A. Marenich; J. Bloino; B. G. Janesko; R. Gomperts; B. Mennucci; H. P. Hratchian; J. V. Ortiz; A. F. Izmaylov; J. L. Sonnenberg; D. Williams-Young; F. Ding; F. Lipparini; F. Egidi; J. Goings; B. Peng; A. Petrone; T. Henderson; D. Ranasinghe; V. G. Zakrzewski; J. Gao, N. R.; G. Zheng, W. L.; M. Hada; M. Ehara; K. Toyota; R. Fukuda; J. Hasegawa; M. Ishida; T. Nakajima; Y. Honda; O. Kitao; H. Nakai; T. Vreven; K. Throssell; J. A. Montgomery, J.; J. E. Peralta; F. Ogliaro; M. Bearpark; J. J. Heyd; E. Brothers; K. N. Kudin; V. N. Staroverov; T. Keith; R. Kobayashi; J. Normand; K. Raghavachari; A. Rendell; J. C. Burant; S. S. Iyengar; J. Tomasi; M. Cossi; J. M. Millam; M. Klene; C. Adamo; Cammi, R.; , J. W. O.; R. L. Martin; K. Morokuma; O. Farkas; J. B. Foresman; and D. J. Fox; , *Gaussian 09*. Gaussian, Inc.: Wallingford, CT, 2009.
(54) Cances, E.; Mennucci, B.; Tomasi, J. A New Integral Equation Formalism for the Polarizable Continuum Model: Theoretical Background and Applications to Isotropic and Anisotropic Dielectrics. *J. Chem. Phys.* **1997,** *107*, 3032-3041.
(55) Cossi, M.; Barone, V.; Mennucci, B.; Tomasi, J. Ab Initio Study of Ionic Solutions by a Polarizable Continuum Dielectric Model. *Chem. Phys. Lett.* **1998,** *286*, 253-260.
(56) Mennucci, B.; Tomasi, J. Continuum Solvation Models: A New Approach to the Problem of Solute's Charge Distribution and Cavity Boundaries. *J. Chem. Phys.* **1997,** *106*, 5151-5158.
(57) Wadt, W. R.; Hay, P. J. Ab-initio Effective Core Potentials for Molecular Calculations - Potentials for Main Group Elements Na to Bi. *J. Chem. Phys.* **1985,** *82*, 284-298.
(58) Hay, P. J.; Wadt, W. R. Ab-initio Effective Core Potentials for Molecular Calculations - Potentials for the Transition-metal Atoms Sc to Hg. *J. Chem. Phys.* **1985,** *82*, 270-283.
(59) Hay, P. J.; Wadt, W. R. Ab-initio Effective Core Potentials for Molecular Calculations - Potentials for K to Au Including the Outermost Core Orbitals. *J. Chem. Phys.* **1985,** *82*, 299-310.
(60) Schreckenbach, G.; Ziegler, T. Calculation of NMR Shielding Tensors Using Gauge-Including Atomic Orbitals and Modern Density-Functional Theory. *J. Phys. Chem.* **1995,** *99*, 606-611.
(61) Krykunov, M.; Ziegler, T.; Van Lenthe, E. Hybrid Density Functional Calculations of Nuclear Magnetic Shieldings Using Slater-Type Orbitals and the Zeroth-Order Regular Approximation. *Int. J. Quantum Chem.* **2009,** *109*, 1676-1683.
(62) te Velde, G.; Bickelhaupt, F. M.; Baerends, E. J.; Guerra, C. F.; Van Gisbergen, S. J. A.; Snijders, J. G.; Ziegler, T. Chemistry with ADF. *J. Comput. Chem.* **2001,** *22*, 931-967.
(63) Van Lenthe, E.; Baerends, E. J. Optimized Slater-type Basis Sets for the Elements 1-118. *J. Comput. Chem.* **2003,** *24*, 1142-1156.
(64) Wolff, S. K.; Ziegler, T. Calculation of DFT-GIAO NMR Shifts with the Inclusion of Spin-orbit Coupling. *J. Chem. Phys.* **1998,** *109*, 895-905.
(65) Wolff, S. K.; Ziegler, T.; van Lenthe, E.; Baerends, E. J. Density Functional Calculations of Nuclear Magnetic Shieldings Using the Zeroth-order Regular Approximation (ZORA) for Relativistic Effects: ZORA Nuclear Magnetic Resonance. *J. Chem. Phys.* **1999,** *110*, 7689-7698.
(66) Conley, M. P.; Rossini, A. J.; Comas-Vives, A.; Valla, M.; Casano, G.; Ouari, O.; Tordo, P.; Lesage, A.; Emsley, L.; Copéret, C. Silica-surface Reorganization During Organotin Grafting Evidenced by Sn-119 DNP SENS: a Tandem Reaction of Gem-silanols and Strained Siloxane Bridges. *Phys. Chem. Chem. Phys.* **2014,** *16*, 17822-17827.
(67) Dai, W.; Wang, C.; Tang, B.; Wu, G.; Guan, N.; Xie, Z.; Hunger, M.; Li, L. Lewis Acid Catalysis Confined in Zeolite Cages as a Strategy for Sustainable Heterogeneous Hydration of Epoxides. *ACS Catal.*, **2016**, *6*, 2955-2964.
(68) Behrens, M.; Schlögl, R. In *Characterization of Solid Materials and Heterogeneous Catalysts: From Structure to Surface Reactivity, Volume 1 & 2*; Che, M.; Vedrine, J. C., Eds.; Wiley: Weinheim, Germany, 2012.
(69) Deimund, M. A.; Harrison, L.; Lunn, J. D.; Liu, Y.; Malek, A.; Shayib, R.; Davis, M. E. Effect of Heteroatom Concentration in SSZ-13 on the Methanol-to-Olefins Reaction. *ACS Catal.* **2016,** *6*, 542-550.
(70) Di Iorio, J. R.; Gounder, R. Controlling the Isolation and Pairing of Aluminum in Chabazite Zeolites Using Mixtures of Organic and Inorganic Structure-Directing Agents. *Chem. Mater.* **2016,** *28*, 2236-2247.
(71) Bermejo-Deval, R.; Gounder, R.; Davis, M. E. Framework and Extraframework Tin Sites in Zeolite Beta React Glucose Differently. *ACS Catal.* **2012,** *2*, 2705-2713.
(72) Thommes, M. Physical Adsorption Characterization of Nanoporous Materials**.** *Chem. Ing. Tech.* **2010**, *82*, 1059-1073.
(73) Vega-Vila, J. C.; Harris, J. W.; Gounder, R. Controlled Insertion of Tin Atoms into Zeolite Framework Vacancies and Consequences for Glucose Isomerization Catalysis. *J. Catal.* **2016,** *344*, 108-120.
(74) Mal, N. K.; Ramaswamy, A. V. Hydroxylation of Phenol over Sn-silicalite-1 Molecular Sieve: Solvent Effects. *J. Mol. Catal. A* **1996,** *105*, 149-158.
(75) Bhagwat, M.; Shah, P.; Ramaswamy, V. Synthesis of Nanocrystalline SnO2 Powder by Amorphous Citrate Route. *Mat. Lett.* **2003,** *57*, 1604-1611.
(76) Chiodini, N.; Paleari, A.; Di Martino, D.; Spinolo, G. SnO2 Nanocrystals in SiO2: A Wide-band-gap Quantum-dot System. *Appl. Phys. Lett.* **2002,** *81*, 1702-1704.
(77) Gu, F.; Wang, S. F.; Song, C. F.; Lu, M. K.; Qi, Y. X.; Zhou, G. J.; Xu, D.; Yuan, D. R. Synthesis and Luminescence Properties of SnO2 Nanoparticles. *Chem. Phys. Lett.* **2003,** *372*, 451-454.
(78) Pang, G. S.; Chen, S. G.; Koltypin, Y.; Zaban, A.; Feng, S. H.; Gedanken, A. Controlling the Particle Size of Calcined SnO2 Nanocrystals. *Nano Lett.* **2001,** *1*, 723-726.
(79) Roy, S.; Bakhmutsky, K.; Mahmoud, E.; Lobo, R. F.; Gorte, R. J. Probing Lewis Acid Sites in Sn- Beta Zeolite. *ACS Catal.* **2013,** *3*, 573.
(80) Sushkevich, V. L.; Ivanova, I. I.; Yakimov, A. V. Revisiting Acidity of SnBEA Catalysts by Combined Application of FTIR Spectroscopy of Different Probe Molecules. *J. Phys. Chem. C* **2017**, *121*, 11437-11447.
(81) Josephson, T. R.; Jenness, G. R.; Vlachos, D. G.; Caratzoulas, S. Distribution of Open Sites in Sn-Beta Zeolite. *Microporous Mesoporous Mater.* **2017,** *245*, 45-50.
(82) Yakimov, A. G.; Kolyagin, Y. G.; Tolborg, S.; Vennestrom, P. N. R.; Ivanova, I. I. 119Sn MAS NMR Study of the Interaction

of Probe Molecules with Sn-BEA: The Origin of Penta- and Hexacoordinated Tin Formation. *J. Phys. Chem. C* **2016,** *120*, 28083-28092.
(83) Zhu, X. C.; Hofmann, J. P.; Mezari, B.; Kosinov, N.; Wu, L. L.; Qian, Q. Y.; Weckhuysen, B. M.; Asahina, S.; Ruiz-Martinez, J.; Hensen, E. J. M. Trimodal Porous Hierarchical SSZ-13 Zeolite with Improved Catalytic Performance in the Methanol-to-Olefins Reaction. *ACS Catal.* **2016,** *6*, 2163-2177.
(84) Palomino, G. T.; Pascual, J. J. C.; Delgado, M. R.; Parra, J. B.; Arean, C. O. FT-IR Studies on the Acidity of Gallium-substituted Mesoporous MCM-41 Silica. *Mat. Chem. Phys.* **2004,** *85*, 145-150.
(85) Luo, H. Y.; Consoli, D. F.; Gunther, W. R.; Román-Leshkov, Y. Investigation of the Reaction Kinetics of Isolated Lewis Acid Sites in Beta Zeolites for the Meerwein-Ponndorf-Verley Reduction of Methyl Levulinate to Gamma-valerolactone. *J. Catal.* **2014,** *320*, 198-207.
(86) Cohen, R.; Graves, C. R.; Nguyen, S. B. T.; Martin, J. M. L.; Ratner, M. A. The Mechanism of Aluminum-catalyzed Meerwein-Schmidt-Ponndorf-Verley Reduction of Carbonyls to Alcohols. *J. Am. Chem. Soc.* **2004,** *126*, 14796-14803.
(87) Assary, R. S.; Curtiss, L. A.; Dumesic, J. A. Exploring Meerwein-Ponndorf-Verley Reduction Chemistry for Biomass Catalysis Using a First-Principles Approach. *ACS Catal.* **2013,** *3*, 2694-2704.
(88) Boronat, M.; Corma, A.; Renz, M. Mechanism of the Meerwein-Ponndorf-Verley-Oppenauer (MPVO) Redox Equilibrium on Sn- and Zr-beta Zeolite Catalysts. *J. Phys. Chem. B* **2006,** *110*, 21168-21174.
(89) Shibagaki, M.; Takahashi, K.; Matsushita, H. The Catalytic Reduction of Aldehydes and Ketones With 2-propanol Over Hydrous Zirconium-oxide. *Bull. Chem. Soc. Jpn.* **1988,** *61*, 3283-3288.
(90) Ordomsky, V. V.; Sushkevich, V. L.; Ivanova, I. I. Study of Acetaldehyde Condensation Chemistry over Magnesia and Zirconia Supported on Silica. *J. Mol. Catal. A* **2010,** *333*, 85-93.
(91) Ivanov, V. A.; Bachelier, J.; Audry, F.; Lavalley, J. C. Study of the Meerwein-Pondorff-Verley Reaction Between Ethanol and Acetone on Various Metal-Oxides. *J. Mol. Catal.* **1994,** *91*, 45-59.
(92) Palagin, D.; Sushkevich, V. L.; Ivanova, I. I. C–C Coupling Catalyzed by Zeolites: is Enolization the Only Possible Pathway for Aldol Condensation? *J. Phys. Chem. C* **2016,** *120*, 23566-23575.
(93) Román-Leshkov, Y.; Moliner, M.; Labinger, J. A.; Davis, M. E. Mechanism of Glucose Isomerization Using a Solid Lewis Acid Catalyst in Water. *Angew. Chem., Int. Ed.* **2010,** *49*, 8954-8957.
(94) Bermejo-Deval, R.; Assary, R. S.; Nikolla, E.; Moliner, M.; Román-Leshkov, Y.; Hwang, S.-J.; Palsdottir, A.; Silverman, D.; Lobo, R. F.; Curtiss, L. A.; Davis, M. E. Metalloenzyme-like Catalyzed Isomerizations of Sugars by Lewis Acid Zeolites. *Proc. Natl. Acad. Sci. USA* **2012,** *109*, 9727-9732.
(95) Gounder, R.; Davis, M. E. Monosaccharide and Disaccharide Isomerization over Lewis Acid Sites in Hydrophobic and Hydrophilic Molecular Sieves. *J. Catal.* **2013,** *308*, 176-188.
(96) Hung, I.; Rossini, A. J.; Schurko, R. W. Application of the Carr-Purcell Meiboom-Gill Pulse Sequence for the Acquisition of Solid-state NMR Spectra of Spin-(1)/(2) Nuclei. *J. Phys. Chem. A* **2004,** *108*, 7112-7120.
(97) Herzfeld, J.; Berger, A. E. Sideband Intensities in NMR-spectra of Samples Spinning at the Magic Angle. *J. Chem. Phys.* **1980,** *73*, 6021-6030.
(98) Gunther, W. R.; Michaelis, V. K.; Griffin, R. G.; Román-Leshkov, Y. Interrogating the Lewis Acidity of Metal Sites in Beta Zeolites With 15N Pyridine Adsorption Coupled With MAS NMR Spectroscopy. *J. Phys. Chem. C* **2016,** *120*, 28533-28544.

TOC GRAPHIC